Global and Planetary Change 234 (2024) 104387

Contents lists available at ScienceDirect

Global and Planetary Change

journal homepage: www.elsevier.com/locate/gloplacha

Impact of *Chondrites* on trace metal distribution in the sapropel S7 (ODP Site 966): Implications for paleoenvironmental and paleoceanographic reconstructions

Ricardo D. Monedero-Contreras [a,*], Francisco J. Rodríguez-Tovar [b], Francisca Martínez-Ruiz [a]

[a] Instituto Andaluz de Ciencias de la Tierra (IACT), CSIC-UGR, Armilla, Spain
[b] Departmento de Estratigrafía y Paleontología, Universidad de Granada, Granada, Spain

ARTICLE INFO

Editor: Dr. Fabienne Marret-Davies

Keywords:
Trace metal
Redox conditions
Chondrites
Deoxygenation
Mediterranean
Sapropel
Paleoceanography

ABSTRACT

Organic-rich deposits are valuable paleo-archives, recording significant paleoceanographic changes linked to past climate variations and marine deoxygenation events. The deposition of organic-rich sediments stops when bottom-water reventilation/oxygenation occurs. This impedes organic matter preservation, enabling macro and micro burrowing-organisms to recover and bioturbate the seafloor. In this sense, highly bioturbated sediments require particular attention when sampling is done for geochemical analyses, as sediments can be considerably mixed. While avoiding trace fossils during sampling for geochemical analyses is easy for large traces (e.g. *Planolites, Thallasinoides,* and *Zoophycos*), it becomes challenging for smaller and complex traces (< 0.5 cm), as is the case with *Chondrites*. *Chondrites*-producers have an opportunistic behavior, being one of the first organisms to colonize the seafloor after an anoxic event. As a result, *Chondrites* are commonly and sometimes abundantly found in the upper layers of organic-rich sediments, including sapropels and black shales.

This study focuses on sapropel S7, which was deposited between ~198.5 and 191.9 ka at the top of Eratosthenes Seamount and exhibits abundant *Chondrites*. For this sapropel, we demonstrated that *Chondrites*-producers can bioturbate significant volumes of organic-rich sediments (over 35%), introducing oxic/dysoxic material downward into anoxic sediments enriched in redox-sensitive trace metals and organic matter. This process can dilute up to 18% the original concentration of redox-sensitive trace metals (e.g. Mo, U and V). This dilution is especially important to consider when calculating trace metals and organic matter burial flux from bulk sediment data. Therefore, *Chondrites*-producers can play a crucial role in altering the sediment texture and distribution of minerals and organic matter at sub-cm scale, and may thus impact paleoenvironmental and paleoceanographic reconstructions based on geochemical signals. Furthermore, the subsequent redistribution of organic matter and redox-sensitive trace metals (including oligoelements) within the sediment can affect carbon and nutrient cycling, microbial activity, organic matter degradation in deep-marine sediments, and the overall sedimentary biogeochemistry.

1. Introduction

Organic-rich deposits are regarded as oceanographic paleo-archives of significant environmental importance because they record profound paleoceanographic changes typically associated with past climate variations. They are valuable tools for comprehending long-term oceanographic responses to contemporary climate change (Hennekam et al., 2020). The combination of sustained surface water eutrophication and water-column stagnation promotes expansion of the O_2-minimum zone into deeper settings and oxygen-depletion in deep bottom-waters, respectively (Zirks et al., 2019). In deep-marine settings, bottom-water deoxygenation leads to enhanced organic matter (OM) preservation and to the authigenic enrichment of redox-sensitive trace metals (RSTMs) such as Mo, U, and V (Tribovillard et al., 2006). Therefore, the concentrations of RSTMs in marine sediments are broadly utilized in geochemical paleoenvironmental studies as proxies for redox conditions (Warning and Brumsack, 2000; Tribovillard et al., 2006; Calvert and Pedersen, 1993, 2007; Algeo and Liu, 2020).

In this context, organic-rich deposits −such as sapropels− represent exceptional records of past deoxygenation events. Sapropels are quasi-

* Corresponding author.
E-mail address: ricardo.monedero@csic.es (R.D. Monedero-Contreras).

https://doi.org/10.1016/j.gloplacha.2024.104387
Received 2 August 2023; Received in revised form 6 February 2024; Accepted 14 February 2024
Available online 15 February 2024

cyclic organic-rich sediments deposited in the Eastern Mediterranean during periods of enhanced productivity and bottom-water restriction (Emeis et al., 2000). Their cyclic deposition is linked to astronomical precession cyclicity, whereby periods of minimum astronomical precession result in maximum insolation in the Northern Hemisphere (Fig. 1c) (Hilgen, 1991; Lourens et al., 1996; Hennekam et al., 2014). This phenomenon triggers the intensification and northward migration of the African monsoon, leading to increased freshwater and nutrient input into the Eastern Mediterranean, and thereby promoting a decrease in surface water salinity and deep-water stagnation and deoxygenation (Weldeab et al., 2014; Tachikawa et al., 2015; Rohling et al., 2015; Wu et al., 2016, 2018; Andersen et al., 2020; Monedero-Contreras et al., 2023a).

Bottom-water deoxygenation ceases once ventilation occurs. Subsequently, during the reactivation of bottom-water circulation, oxygenated waters reach the seafloor and inhibit the accumulation/preservation of organic-rich sediments, as is the case during sapropel termination (Pruysers et al., 1991, 1993; Reitz et al., 2006; de Lange et al., 2008; Filippidi and de Lange, 2019). During bottom-water reoxygenation, both macro and micro benthic organisms rapidly colonize and repopulate the seafloor (Löwemark et al., 2006). Opportunistic burrowing organisms penetrate the underlying organic-rich sediments, leading to two potential outcomes: (i) discrete traces with marked outlines and differentiated infill, or (ii) a total remobilization and mixing of the sediment, determining a mottled background, consisting of biodeformational sedimentary structures, having no distinct outline (Rodríguez-Tovar, 2022). In either case, these processes may alter the original concentrations of RSTMs within the organic-rich sediment. Consequently, bioturbation is seen as a crucial factor when assessing RSTM concentrations in paleoenvironmental and paleoceanographic

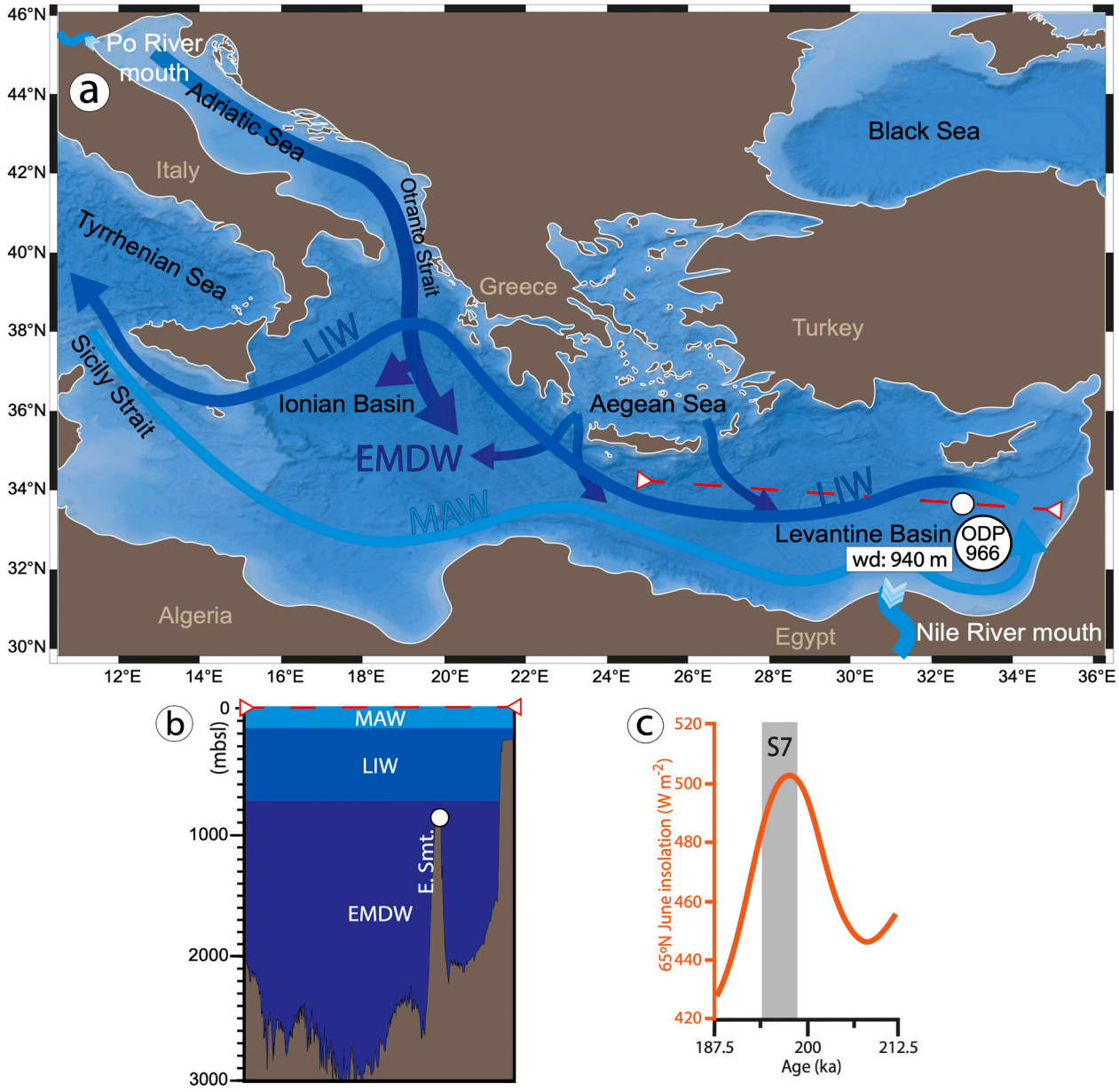

Fig. 1. (a) Base map generated using GeoMapApp, showing location of core 966B, Eastern Mediterranean circulation pattern and the superficial expression of the bathymetric transect. (b) Bathymetric transect obtained by European Marine Observation Data Network (EMODnet) (http://www.emodnet-seabedhabitats.eu/). Location and depth of core 966B are indicated as a white circle at the top of Eratosthenes Seamount (E. Smt.). Eastern Mediterranean water-masses are indicated. Modified Atlantic Water: WAW, Levantine Intermediate Water: LIW, Eastern Mediterranean Deep Water: EMDW. (c) S7 time interval (198.5–191.9 ka) based on Ziegler et al. (2010; 65°N summer insolation curve (in orange) from Laskar and Boudin (1993).

reconstructions. It is therefore essential to identify trace fossils to avoid the infilling material when sampling for geochemical analyses. Trace fossils are often visually distinguishable in organic-rich sediments due to their contrasting coloration when compared to the host sediment. Larger trace fossils frequently registered in deep-marine environments, such as *Planolites*, *Thallasinoides*, and *Zoophycos* (Rodríguez-Tovar, 2022), can usually be avoided during sampling for geochemical analyses. However, the same cannot be said for smaller trace fossils (< 0.5 cm), such as *Chondrites*, which are also very common in deep-marine environments and exhibit highly complex architecture (Baucon et al., 2020).

Chondrites normally exhibit a branching tunnel system, as a dendritic network, consisting of a small number of sub-vertical burrows, connected to the paleosediment-water interface (Baucon et al., 2020 and reference therein). *Chondrites*-producers exhibit opportunistic behavior, often being one of the first tracemakers to bioturbate the seafloor just after an anoxic event, e.g. a sapropel event (Löwemark et al., 2006; Löhr and Kennedy, 2015). Monogeneric or low-diversity assemblages with *Chondrites* are associated with dysoxic environments (Bromley and Ekdale, 1984; Bromley, 1996; Buatois and Mángano, 2016; Baucon et al., 2020). The producers of *Chondrites* appear to be capable of colonizing environments characterized by oxygen levels unfavorable for other tracemakers (Savrda and Bottjer, 1984; Löhr and Kennedy, 2015), being considered as an "extremotolerant" ichnotaxon (Baucon et al., 2020). As a result, they are frequent or even, in some cases, abundant in organic-rich sediments (see Baucon et al., 2020 for a review). This trace has been registered in black shale sediments through the fossil record linked to oceanic anoxic events such as the End Permian Mass Extinction (Rodríguez-Tovar et al., 2021), the Toarcian Oceanic Anoxic Event (Early Toarcian; i.e., Bromley and Ekdale, 1984; Rodríguez-Tovar and Uchman, 2010; Montero-Serrano et al., 2015; Fernández-Martínez et al., 2021; Rodríguez-Tovar, 2021a, 2021b), the Bonarelli Event (Cenomanian-Turonian boundary; Schönfeld et al., 1991; Hilbrecht and Dahmer, 1994; Uchman et al., 2008, 2013a, 2013b; Rodríguez-Tovar et al., 2009a, 2009b, 2020; Rodríguez-Tovar and Uchman, 2011; Monaco et al., 2012, 2016), and the Faraoni Event (upper Hauterivian; Rodríguez-Tovar and Uchman, 2017).

Chondrites-producers can introduce significant volumes of overlying sediments downward into deeper sediments of different composition (Baucon et al., 2020). Discrete bulk sediment samples collected from organic-rich sediments with abundant *Chondrites* will exhibit a mixed geochemical signal resulting from the composition of both *Chondrites* infills and host sediments. Therefore, the RSTM concentrations obtained from bulk sediment samples do not reflect the syndepositional concentrations. Carbon isotope analysis of trace fossil infills —including *Chondrites* — at the Agost section in southern Spain was used to distinguish between different phases of macrobenthic colonization during the K-Pg boundary period (Rodríguez-Tovar et al., 2004, 2006). Yet there are not many studies that specifically assess bioturbation impact on RSTM distribution and concentration within the sediment.

In this context, paleoenvironmental and paleoceanographic reconstructions require the assessment of *Chondrites'* influence on the original concentrations of RSTMs in organic-rich sediments that represent past deoxygenation events. The influence of *Chondrites* on the sub-cm distribution of RSTMs and OM in organic-rich sediments is examined in sapropel S7, deposited at the top of Eratosthenes Seamount. The aim of this study is to demonstrate the important role of discrete traces, particularly *Chondrites,* when using TMs as paleoceanographic proxies, while also assessing their potential impact on sedimentary biogeochemistry.

1.1. Assessed trace metals

Under oxygen-deficient conditions in marine systems, diverse authigenic minerals can precipitate, leading to the enrichment of marine sediments in RSTMs such as Mo, U, V, Re, Cu, Co, Ni, Cr, Zn, Pb, and Mn. Normalizing these metals allows them to be used as redox proxies, to infer different redox conditions in ancient marine environments (Berner, 1981; Calvert and Pedersen, 1993, 2007; Crusius et al., 1996; Tribovillard et al., 2006, 2008; Algeo and Tribovillard, 2009; Scheiderich et al., 2010; Little et al., 2015; Paul et al., 2023). In this study, we focus on the assessment of trace elements Mo, U, V, Co, Cu, Ni, Cr, Zn, Pb, and Ba, which are normally enriched in sapropel layers. Under oxygen-depleted conditions, Mo, V, Co, Cu, Ni, Cr, Pb, and Zn are scavenged from the water-column by manganese (Mn) and iron (Fe) oxyhydroxides, as well as OM, and are subsequently deposited on the seafloor (Scholz et al., 2017). If euxinic conditions occur in the bottom-water or porewaters, these metals become permanently fixed through association with pyrite (FeS) or by forming their own sulfides (e.g. MoS, CuS, CuS_2, NiS, and [Zn,Fe]S, CoS, NiS) or oxides in the case of V (e.g. V_2O_3) (Tribovillard et al., 2006 and references therein). U behaves differently, as it is not influenced by the redox cycling of Mn and Fe in the water-column. Instead, U precipitates as the less soluble lower oxidation state in association with humic and fulvic acids derived from OM degradation during anoxic conditions in bottom-waters (Zheng et al., 2002; McManus et al., 2005; Morford et al., 2005; Tribovillard et al., 2006; Calvert and Pedersen, 2007).

The Ba in sapropel sediments is primarily attributed to an increase in the abundance of marine barite (Martínez-Ruiz et al., 2000). The precipitation of barite in the water-column has been linked to periods of heightened productivity and degradation of OM in the mesopelagic zone (Bishop, 1988; Paytan et al., 2002, 2004; Calvert and Pedersen, 2007; Paytan and Griffith, 2007; Gallego-Torres et al., 2007a, 2010; Martínez-Ruiz et al., 2020; Filippidi and de Lange, 2019). Martínez-Ruiz et al. (2018, 2019) have demonstrated the significant role of bacteria and particularly Extracellular Polymeric Substances in promoting saturated microenvironments in which Ba precipitates. Due to its correlation with productivity, the Ba content is commonly employed as a qualitative proxy for assessing past oceanic productivity. Consequently, in this study, the potential Ba dilution resulting from the remobilization of *Chondrites* sediments was also evaluated.

2. Paleo-oceanographic setting and sediment record

The studied sediment record, containing the sapropel S7, was retrieved in 1995 during the Ocean Drilling Program (ODP) Leg 160 expedition at Site 966-Hole B, hereafter referred to as Site 966B (see Emeis et al., 1996 for Leg 160 expedition scientific report). Site 966B (33°47.765′N, 32°42.090′E) is located near the northern margin of the Eratosthenes Seamount plateau, at a depth of 927 m below sea level (mbsl) (Fig. 1a and b). At present, circulation in the Eastern Mediterranean is controlled by two main mechanisms: wind stress and thermohaline forcing (POEM Group, 1992; Millot and Taupier-Letage, 2005; Amitai et al., 2018). The Eratosthenes Seamount lies beneath the present-day Levantine Intermediate Water (LIW) (Fig. 1a and b). The depth of Site 966B corresponds to the lower limit of MIW and the upper limit of Eastern Mediterranean Deep-Water (EMDW), around 1000 mbsl (Wüst, 1961). Despite the close proximity of Eratosthenes Seamount to the Nile River mouth, Site 966B is not affected by fan deposition from the Nile Cone, and is not influenced by downslope gravity processes that could disturb the sediment record (Emeis et al., 1996). However, during sapropel events, the water-column structure and current dynamics differed significantly from those observed in the modern Eastern Mediterranean. Specifically, sapropel event S7 occurred between 198.5 and 191.9 ka, during Marine Isotope Stage 7a (Fig. 1c; Ziegler et al., 2010). This period, in the Eastern Mediterranean, was characterized by exceptionally intense African monsoons and high freshwater input, which resulted in high marine productivity, stable water-column stratification, and anoxic/euxinic EMDW (Gallego-Torres et al., 2007a; Benkovitz et al., 2020; Sweere et al., 2021; Monedero-Contreras et al., 2023a).

The 966B sediment record consists mainly of nannofossil clay, clayey nannofossil ooze, and nannofossil ooze, with characteristic layers that

Table 1
Major element concentrations (wt%), TMs concentrations (μg/g), TOC (%) and calculated DOPt values obtained from geochemical analyses of bulk sediment samples. S7 subsections are indicated.

				ICP-MS (μg/g)										ICP-OES (wt%)							
	Depth (cm)	TOC (%)	DOPt	Ba	V	Co	Cr	Ni	Cu	Mo	U	Zn	Pb	Al	Ca	Fe	K	Mg	Mn	S	Ti
	470.0	0.49	0.21	260	67	16	58	56	45	1	4	55	9	3.68	17.62	2.52	0.96	1.60	0.04	0.61	0.28
	472.0	0.21	0.24	286	68	14	56	48	56	2	3	55	9	3.70	16.81	2.55	0.98	1.48	0.04	0.71	0.28
	474.0	0.89	0.09	265	68	16	59	55	56	3	3	56	9	3.74	16.29	2.38	0.95	1.59	0.04	0.25	0.28
	477.0	0.28	0.04	326	78	13	71	52	27	3	3	58	10	4.35	13.96	2.79	1.05	1.56	0.04	0.13	0.32
	479.0	2.04	0.12	616	96	20	93	76	88	7	4	72	9	4.30	14.37	2.95	0.98	1.35	0.04	0.40	0.28
	481.0	3.43	0.33	660	119	31	73	113	85	26	5	67	8	4.19	13.91	3.67	0.92	1.27	0.04	1.39	0.27
	482.0	3.01	0.32	736	157	35	67	120	76	51	8	65	9	4.15	13.96	4.66	0.96	1.29	0.04	1.69	0.27
S7b section	484.0	2.32	0.13	557	208	33	70	106	67	27	7	69	10	4.52	12.57	3.47	1.05	1.45	0.04	0.53	0.31
	486.0	2.87	0.19	582	204	37	75	127	73	53	9	70	11	4.81	11.86	3.36	1.11	1.49	0.04	0.74	0.33
	488.0	1.76	0.12	567	185	30	71	103	65	47	7	65	11	4.53	13.49	3.21	1.07	1.56	0.05	0.45	0.32
	489.5	1.88	0.11	544	202	33	76	112	72	16	9	73	11	4.86	12.37	3.30	1.09	1.53	0.04	0.41	0.34
	491.0	1.79	0.16	371	194	24	80	91	63	20	7	64	10	4.98	11.99	3.03	1.05	1.43	0.03	0.57	0.32
	493.0	0.78	0.12	422	110	21	68	71	51	4	6	67	11	4.54	14.75	3.24	1.07	1.56	0.04	0.46	0.33
	494.5	0.80	0.23	418	101	22	69	77	51	14	6	69	10	4.50	14.74	3.31	1.05	1.54	0.04	0.87	0.32
	496.0	0.97	0.14	391	104	19	72	70	58	7	5	64	10	4.45	13.59	2.90	1.00	1.42	0.03	0.46	0.30
S7a section	498.0	0.81	0.20	412	103	21	68	70	51	4	5	65	10	4.43	14.47	3.00	1.04	1.55	0.04	0.67	0.31
	500.0	0.34	0.15	300	103	21	69	73	48	10	5	57	9	4.15	14.53	2.73	0.95	1.58	0.04	0.48	0.29
	501.0	0.98	0.13	365	121	22	67	77	53	8	5	64	10	4.39	14.52	3.10	1.03	1.64	0.05	0.45	0.32
	503.5	1.53	0.29	312	116	26	68	88	55	14	5	61	9	4.08	14.42	3.15	0.94	1.52	0.04	1.06	0.28
	505.5	0.45	0.34	123	66	19	48	55	37	6	3	49	7	3.07	18.28	2.41	0.80	1.78	0.05	0.94	0.23
	507.0	0.22	0.24	97	67	18	41	47	35	4	3	44	7	2.87	20.23	2.26	0.77	2.05	0.05	0.62	0.21
	509.0	0.18	0.11	91	65	17	49	49	44	2	3	47	8	3.19	18.36	1.91	0.82	1.81	0.05	0.24	0.24
	511.0	0.16	0.39	87	59	24	40	59	34	2	3	44	7	2.97	19.28	3.36	0.79	2.02	0.05	1.50	0.23
	512.0	0.16	0.11	110	70	18	48	51	29	2	3	52	8	3.42	18.82	2.37	0.90	2.02	0.06	0.29	0.27
	514.0	0.32	0.14	90	61	16	46	47	32	1	2	44	7	3.20	18.90	2.13	0.81	1.90	0.05	0.34	0.24

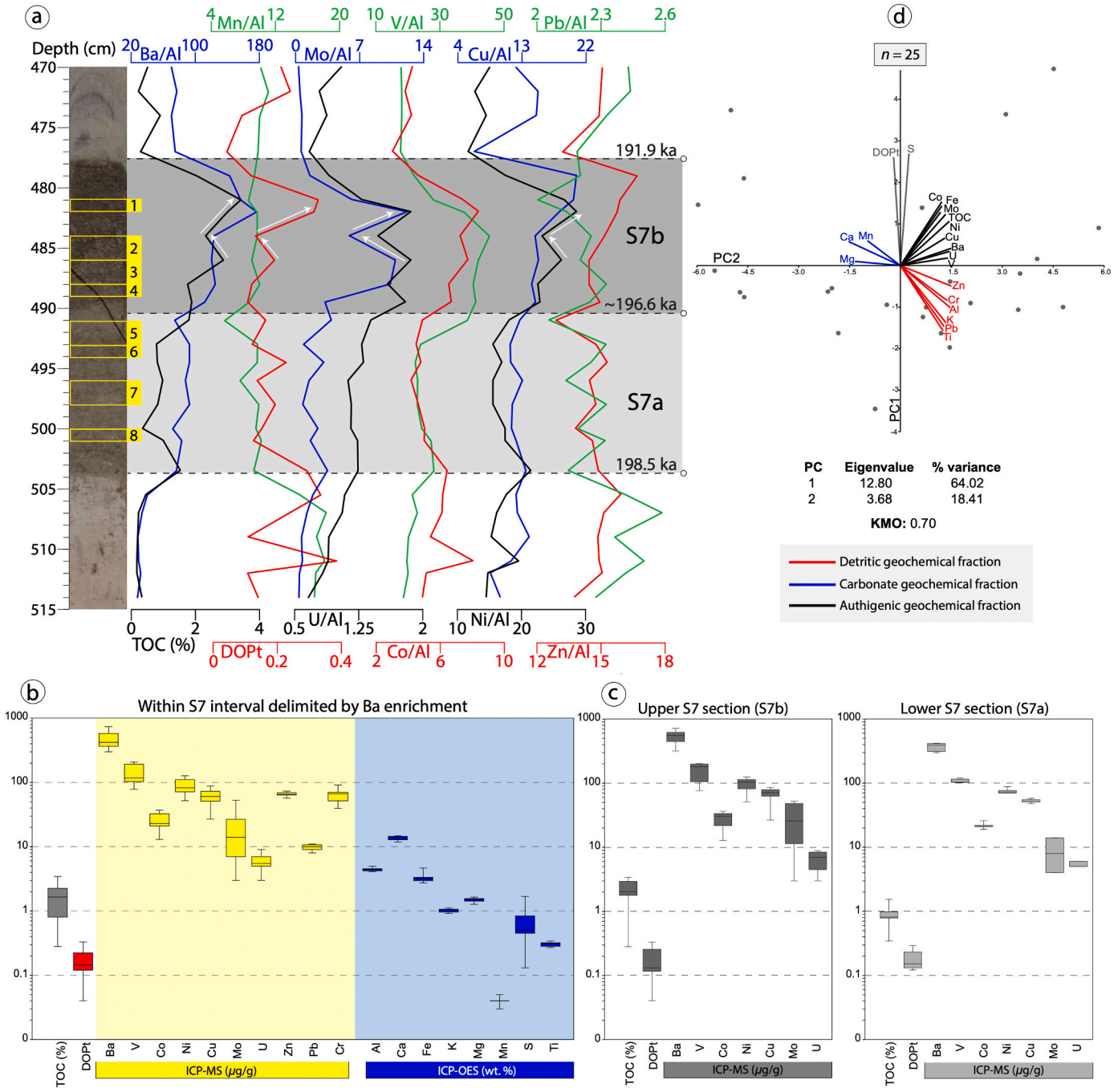

Fig. 2. Results of geochemical analyses of bulk sediment samples. (a) Vertical plots of Al-normalized TMs concentrations ([TM]/[Al] x10^{-4}), TOC (%) and DOPt values. S7a and S7b subsections are indicated. Selected samples for thin-section preparation are indicated on the core image as yellow boxes. (b) Box-plots of major elements and TMs concentrations, TOC (%) and DOPt values within interval S7 delimited by Ba enrichment. (c) Box-plots of TMs concentrations, DOPt and TOC (%) of S7: top half (section S7b) and S7 bottom half (section S7a). All box-plots are presented in $\log_{10}$ scale. (d) Principal Components scatter-plot (PC1: y-axis, PC2: x-axis) with a biplot projection of the variables. This allowed for a visual establishment of the main geochemical affinities and fractions in S7 sediments. Identified geochemical fractions are shown in different Eigenvalues, and variance (%) values of PC1 and PC2 are indicated. For details on Principal Components Analysis and the Kaiser-Meyer-Olkin Test (KMO) value see to section 3.6. For additional geochemical information about S7 at Site 966B, including calculated enrichment factors of assessed trace metals, consult Monedero-Contreras et al. (2024). (For interpretation of the references to color in this figure legend, the reader is referred to the web version of this article.)

include foraminiferal sandy levels, discrete tephra layers, and sapropels (dark layers) (Emeis et al., 1996, 2000). The 45 cm studied interval – spanning from 515 to 470 cm in core section 966B 1H-4– includes sediments from sapropel S7, as well as underlying and overlying sediments. The interval was sampled at 1–3 cm resolution, with a total of 25 discrete sediment samples for geochemical analyses (i.e. Rock- Eval, ICP-OES and ICP-MS; refer to section 3.1) (Table 1). From this interval, eight samples belonging to S7 sediments were selected for sediment thin-section preparation. The sediment thin-sections were prepared by embedding 1–2 cm sediment samples in resin, and then slicing them into ~100 µm thick sections (Fig. 2a). Sediment thin-sections were used for: (i) high-resolution images, (ii) bioturbation quantification, (iii) Laser ablation-ICP-MS analyses (LA-ICP-MS), and (iv) Scanning Electron Microscopy (SEM) observations.

3. Methodology approach

3.1. Geochemical analyses

Total organic carbon (TOC) content was measured in the 25 sediment samples by means of the Rock-Eval pyrolysis method, at the Institute of Earth Sciences (ISTE) of the University of Lausanne (UNIL). This method involved heating the samples from 200 °C to 850 °C in successive steps in a pyrolysis oven with an inert atmosphere (N_2). TOC (%) is calculated from the obtained thermograms using the following equation: TOC (%) = Pyrolyzed Carbon (wt%) + Residual Carbon (wt %). Samples were calibrated using the IFP160000 standard with an instrumental precision of <0.1 wt% for TOC (Lafargue et al., 1998; Behar et al., 2001; Ordoñez et al., 2019).

ICP-MS and ICP-OES analyses were carried out at the Scientific Instrumentation Center of the University of Granada. For ICP analyses, discrete sediment samples were oven-dried at 60 °C and then powdered in an agata mortar. The 25 Samples were processed in one batch and an analytical blank was added. Solutions for ICP analyses were prepared using 0.1 g of powdered sample in Teflon vessels, where successive acidifications using HNO_3 (69%) and HF (48%) were performed at 130 °C until evaporation. A final acid digestion with HNO_3 (69%) and water at 80 °C for 1 h was performed to achieve a total acid dissolution of the sediment samples. Subsequently, dissolved samples were diluted with Milli-Q water in 100 ml flasks following standard procedures (Bea, 1996).

Major elements in discrete sediment samples were measured with an Inductively Coupled Plasma Optical Emission Spectroscopy (ICP-OES) Perkin-Elmer Optima 8300 (Dual View) with a Perkin-Elmer autosampler. Certified standards (BR-N, GH, DR-N, UB-N, AGV—N, MAG-1, GS-N, and GA) were measured for element quantification. Trace elements in discrete sediment samples were measured by Inductively Coupled Plasma Mass Spectrometry (ICP-MS) – NexION 300d (Perkin Elmer) spectrometer– using Rh as the internal standard. For major elements, ICP-OES precision was better than 1%. For trace elements, ICP-MS precision was close to 2% and 5%, respectively on concentrations of 500 μg/g and 5 μg/g (Bea, 1996). Trace metals were normalized with aluminum (TM/Al) due to its conservative properties and since it is considered an optimal method for evaluating trace metal variability (Tribovillard et al., 2006; Calvert and Pedersen, 2007; Algeo and Li, 2020; Algeo and Liu, 2020; Paul et al., 2023).

LA-ICP-MS is known to have high potential for reliable quantitative analysis of diagnostic trace elements (e.g. Mo, V, U and Ba) in (laminated) resin-embedded sediments (Jilbert et al., 2008, 2010; Hennekam et al., 2015; Sosa-Montes de Oca et al., 2018). Therefore, trace element concentrations in selected locations on the sediment thin-sections were determined by laser ablation (LA-ICP-MS) at the Scientific Instrumentation Center, University of Granada. The LA-ICP-MS analyses were performed using a 213 nm Mercantek Nd-YAG laser coupled to an NexION 2000b quadrupole ICP with a shielded plasma torch. The ablation was carried out in a He atmosphere, with a laser beam fixed at 60 μm diameter. The spot was pre-ablated for 45 s at a laser repetition rate of 10 Hz and 20% output energy. A NIST-610 glass was employed as an external standard (see Pearce et al., 2007 for NIST-610 details). In each analytical session of a single thin-section, the NIST-610 glass was analyzed at the beginning and at the end, and also after every nine spots to correct for drift. Concentration values were corrected using silicon as an internal standard. The precision, calculated on five to seven replicates of the NIST-610 glass measured in every session, was in the range of 3% to 7% for most elements. Data reduction was carried out using software written by F. Bea (freely available upon request) in STATA programming language (StataCorp, 2007). Further details on LA-ICP-MS analysis can be found in Bea et al. (2005).

The locations of punctual analyses (i.e. spots) performed on each sample were visually determined using the high-resolution images. Because the aim of these analyses is to compare the geochemical composition of the host sediments versus the *Chondrites* infill material, the analyzed spots were selected and grouped as: (i) host sediment analyses (blue dots in Figs. 10 and 12), and (ii) *Chondrites* infills (red dots in Figs. 10 and 12) in each sample. It is worth mentioning that no LA-ICP-MS analyses were performed in areas where coring disturbances were observed. Refer to Figs. 10–12 for statistical details of LA-ICP-MS punctual analyses of sediment thin-sections.

3.2. High-resolution images

High-resolution images of sediment thin-sections were captured using a Sony Alpha 7 MII camera attached to a Schneider-Kreuznach 50 mm Componon-S f 2.8 enlarging lens and closed bellows between the camera and lens. The high-resolution images were taken at the Scientific Instrumentation Center, University of Granada, by means of an automated motorized "Stack and Stitch" system designed for high-resolution panoramic views. This system utilizes focus stacking methods, combining a series of digital images captured from various quadrants and depths (i.e., focus levels) of the sediment thin-section. Utilizing a computer program, these images are merged to create a panoramic view of the entire thin-section offering exceptional high-definition. Consequently, the stacked and stitched gigapixel macro images can be zoomed into without a loss of resolution and pixelation, providing detailed insights into *Chondrites* disturbances and infills. In this specific case, the stacks were made every 80 μm and each panoramic image comprised ~25 photos, each photo being made up of 100 stacked images. The thin-section images are therefore made from ~2500 photos.

3.3. Bioturbation quantification

The quantification of bioturbation is a key feature of any ichnological analysis, traditionally accomplished through the use of indices such as the bioturbation index (%), assessed by visual observation (Taylor et al., 1993). This implies that the assignment of the percentage of bioturbated area is, to some extent, subjective and semi-quantitative. However, by employing digital image processing techniques based on pixel analysis, an objective quantification of bioturbated areas can be achieved, thus enhancing the reliability of the assigned degree of bioturbation (Dorador et al., 2014a; Dorador and Rodríguez-Tovar, 2017; Dorador and Rodríguez-Tovar, 2015, 2018).

Firstly, the images were cropped to exclude border regions where sediments were disturbed during coring. Discrete traces in the high-resolution images were then visually enhanced by adjusting optical parameters (e.g. contrast and brightness) using Adobe Photoshop CS6 software, following the methodology described by Dorador et al. (2014b). Once the visibility of traces was improved, the number of pixels corresponding to *Chondrites* and the pixels associated with the host sediment were separately determined (Table S1 in Supplementary Material). The percentage of bioturbated areas was calculated as in Dorador et al. (2014a). "Similar Pixel Selection Method (SPSM)," was employed for pixel selection and subsequent quantification of bioturbation by *Chondrites*. For further details on image processing and digital bioturbation quantification, see Dorador et al. (2014a).

3.4. Scanning electron microscope (SEM) imaging and compositional maps

After capturing high-resolution optical images and conducting LA-ICP-MS analyses, sediment thin-sections were coated with carbon for detailed observation under the SEM using an AURIGA FIB-FESEM Carl Zeiss SMT microscope at the Scientific Instrumentation Center of the University of Granada. The SEM is equipped with various detectors, including an EDX (energy dispersive X-ray) detector system from Oxford Instruments, SE (secondary electrons), SE-inLens, BSE (backscattered secondary electrons), EsB (energy selective backscattered electrons) and STEM (scanning transmission electron microscopy) detectors. EDX

served to obtain punctual microanalyses and compositional maps and profiles of major elements in selected areas of the sediment thin-sections. A composite EDX map was generated considering qualitative concentrations of Al, Si, Mg, Fe, S and Ca. Moreover, BSE images of selected areas were captured to facilitate comparison with the high-resolution optical images.

3.5. Data presentation and statistical analyses

Al-normalized trace metals (i.e., [trace metal]/[Al]) is the optimal normalization method to evaluate trace metal variability given the conservative behavior of Al in marine sediments (Paul et al., 2023). Consequently, for temporal and correlative assessment, trace metals concentrations in discrete samples were Al-normalized and then vertically plotted (Fig. 2). Degree of pyritization (DOPt) values were also vertically plotted. This value indicates the abundance of authigenic pyrite in the sediments and it was calculated through the following equation: $DOPt = S_t \times (55.85/64.12) / Fe_t$: where S_t: total sulfur (%), Fe_t: total iron, and the coefficient 55.85/64.12 represents the weight ratio of Fe/S in stoichiometric pyrite (Algeo and Li, 2020; Algeo and Liu, 2020).

Statistical analyses and box-plots were derived with the software PAST 4.0 (Hammer et al., 2001). Box-plots were used to compare major and trace elements concentrations (i) among different S7 subsections and (ii) between *Chondrites* infills and host sediments. Principal Components Analysis (PCA) was performed on the geochemical data obtained from discrete bulk sediments analyses ($n = 25$). The concentrations of Al, Si, Mg, Fe, K, Ca, Sr, Ti, Mn, S, Mo, U, V, Co, Cu, Ni, Zn, Pb, Cr, Ba, as well as DOPt and TOC (%) values, in S7 and surrounding sediments, were introduced in the PCA in order to obtain the main geochemical fractions in S7 sediments and elucidate the trace metals that are mainly enriched in the authigenic fraction. It is important to highlight that PCA was performed using non-normalized elements concentrations, ensuring there were no pre-induced correlations that could mask the real affinities and associations of the variables under assessment.

The PCA eigenvalues and eigenvectors were obtained from the correlation matrix, with the Singular Value Decomposition algorithm. A correlation matrix was used instead of a variance-covariance matrix because the variables are in different units; this implies normalizing all variables through division by their standard deviations (Hammer et al., 2001). The percentages of variance accounted for by Principal Component 1 (PC1) and Principal Component 2 (PC2) are given in Fig. 2e, along with a scatter-plot for a 'Biplot' projection of the variables. The scatter-plot shows all data points plotted in the coordinate system given by PC1 and PC2. A Biplot projection of the original axes (variables) is shown onto the scatter-plot, facilitating visual assessment of any affinities among the variables. This procedure made it possible to identify subsets of components having similar relative variation patterns, which ultimately represent the main geochemical fractions in S7 sediments. Additionally, a Kaiser–Meyer–Olkin (KMO) test was conducted to determine the suitability of the data for factor analysis, assessing whether the variables are interrelated enough to state meaningful interpretations. The KMO test produces a value between 0 and 1, a higher KMO value indicating that the variables are better suited for factor analysis (refer to Fig. 2e for KMO value).

To assess the influence of *Chondrites* bioturbation on the dilution of RSTMs within the organic-rich sediments, a qualitative dilution factor (df) was computed. It is noteworthy that the method for calculating this dilution factor of RSTMs by *Chondrites* bioturbation has not been proposed by previous studies, presenting a novel approach in the field. The calculation assumes that the median trace metal concentrations of the host sediment represent the syndepositional concentrations. Thus, the calculated df provides an estimation of the extent to which RSTMs are diluted by *Chondrites* in the organic-rich sediments. To obtain the df, a weighted average concentration ([wTM]) for each trace metal in every sample was determined, considering the *Chondrites* area (*Ch*%), host sediment area (hs%), median trace metal concentration in *Chondrites* infills ($[TM]_{Ch}$), and median trace metal concentration in host sediments ($[TM]_{hs}$). The formula to calculate [wTM] is as follows: $[wTM] = (([TM]_{hs} * hs\%) + ([TM]_{Ch} * Ch\%)) / 100\%$. The median was chosen over mean/average since it is less influenced by extreme values. The df is then calculated from the difference between the weighted average trace metal concentration, which considers *Chondrites* area, and the median trace metal concentration in the host sediment: $df\% = (([TM]_{hs} - wTM]) / [TM]_{hs})*100$.

4. Results

The top and bottom boundaries of sapropel S7 were determined in view of the Ba/Al trend (Fig. 2a). The Ba/Al ratio serves to determine the original sapropel productivity signal if, eventually, OM is oxidized during reventilation (Gallego-Torres et al., 2007a, 2007b; Filippidi and de Lange, 2019; Monedero-Contreras et al., 2024). Barite ($BaSO_4$), the primary host mineral for Ba, is less prone to postdepositional oxidation as compared to TOC, and the stable sulfate saturation in Eastern Mediterranean porewater enables its preservation during periods of oxygen-depleted bottom-waters (van Os et al., 1991; Passier et al., 1997; Nijenhuis et al., 1999; Martínez-Ruiz et al., 2000). This approach enabled the identification of the original thickness of the organic-rich interval of sapropel S7, even considering potential postdepositional oxidation. To this regard, the S7 interval is identified between 477 and 503.5 cm at Site 966B (Fig. 2). Yet Ba/Al and TOC exhibit similar vertical trends, decreasing simultaneously at the top of S7, indicating that no relevant postdepositional oxidation occurred after S7 termination (Fig. 2a). Therefore, in this case, TOC can also delimit the original thickness of S7.

The S7 interval is enriched in RSTMs such as Mo, U, V, Co, Cu, and Ni, and depleted in Mn (Fig. 2a and b; Table 1). Moreover, Mo, U, V, Cu, Co and Ni have similar vertical plots, while Pb and Zn differ from the rest and do not show significant enrichments (Fig. 2a). Among the RSTMs, Mo exhibits the highest variability (i.e., highest standard deviation) within S7, whereas U has the lowest variability and the lowest concentration (Fig. 2b). V presents the highest concentrations within S7 among the RSTMs (Fig. 2b). However, it is not the most proportionally enriched RSTM relative to the background values (i.e. concentrations before the onset of S7). In this sense, Mo appears to be the RSTM that is most proportionally enriched relative to the background values, as it can increase by up to 1500% assuming background values of 3 μg/g. Interestingly, DOPt increases at the top and bottom of S7, where it reaches DOPt values around 0.3 (Fig. 2a and Table 1).

According to the vertical plots and mean concentration of trace metals and TOC, sapropel S7 can be subdivided into two sections, S7a and S7b (refer to Fig. 2 and Table S3 in Sup. Mat.) Section S7a has lower mean concentrations of RSTMs and Ba than section S7b (Fig. 2c), indicating a change in bottom-water conditions during its deposition. Moreover, in section S7a (from 491 to 477 cm; Fig. 2a), the mean TOC is relatively low (<1%). In section S7b (from 503.5 to 491 cm; Fig. 2a), the TOC is higher (>3%) with mean values above 2% and presents a much lower variability in RSTMs concentration and Ba than section S7b (Figs. 2c and Table 1). The increase in TOC content is also made evident by the darkening of the sediments in the upper S7 half (i.e. from 491 to 479 cm depth; Fig. 2a). See Fig. 2. for more detailed results.

According to PCA, the PC1 and PC2 group >82% of the total variance. The KMO test gives a value of 0.7, indicating the data introduced in the PCA present a "good" adequacy for factor analysis (Fig. 2d). The PCA analysis suggests that there are three main geochemical fractions in S7 sediments: (1) the detritic fraction, enriched in Al, Si, K, Ti, Cr, Zn and Pb, (2) the carbonate fraction, enriched in Ca, Mg and Mn, and (3) the authigenic fraction, enriched in Mo, U, V, Co, Cu, Ni, Ba, Fe and TOC. Even though pyrite is an authigenic mineral, in the authigenic fraction, pyrite is not well correlated with the rest of the RSTMs. Only the trace metals that are mainly enriched in the authigenic fraction (i.e., Mo, U, V, Co, Cu, Ni and Ba) are assessed in the comparison between *Chondrites*

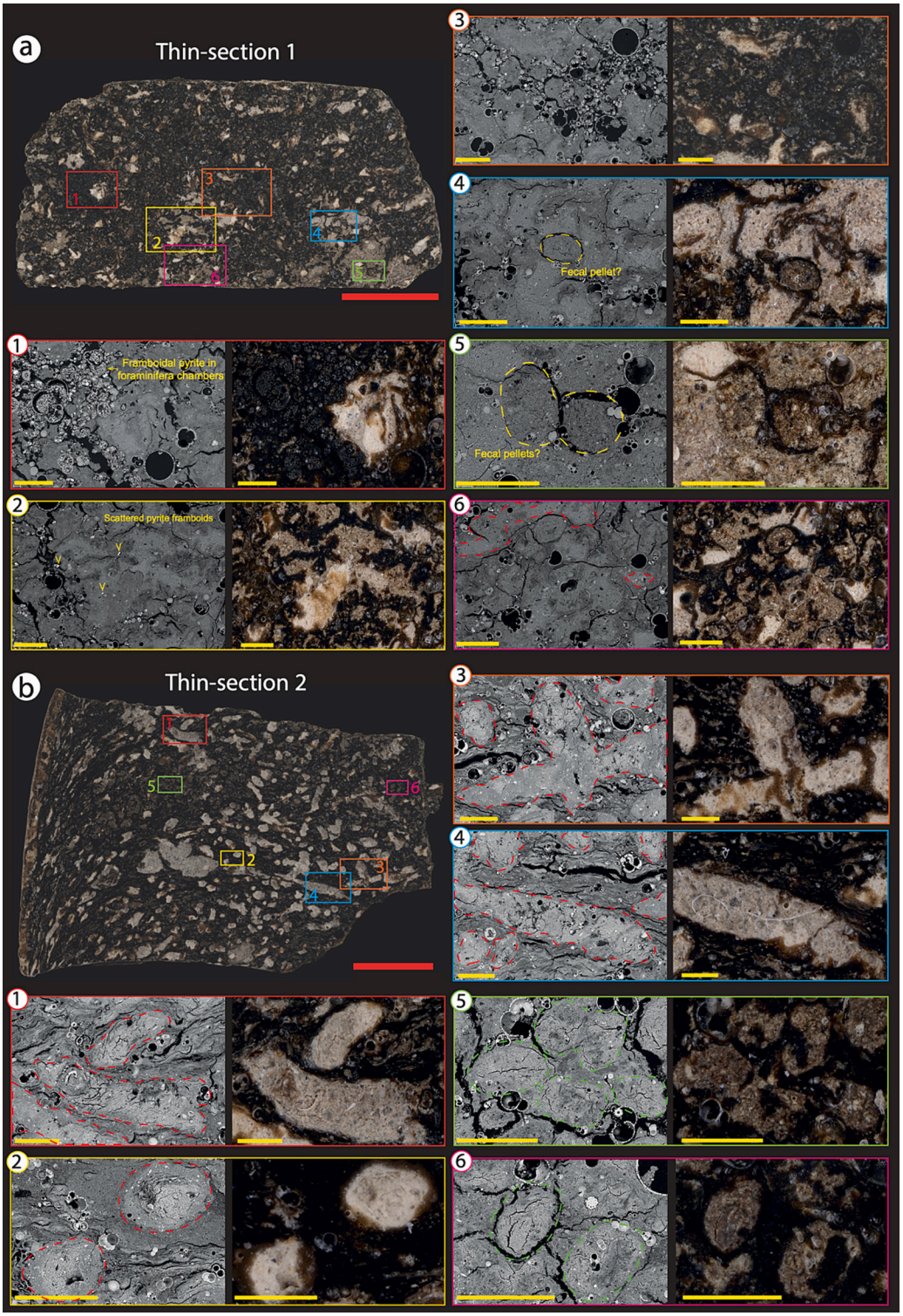

Fig. 3. High-resolution optical images of thin-sections 1 and 2, plus SEM images of selected areas (1–6). Red scale-bar: 5 mm; yellow scale-bar: 0.5 mm (500 μm). The amplified sections are shown as rectangles, each assigned a different color: (1) red, (2) yellow, (3) orange, (4) blue, (5) green, (6) magenta. White *Chondrites* are outlined with red dashed lines and dark *Chondrites* in green dashed lines. (For interpretation of the references to color in this figure legend, the reader is referred to the web version of this article.)

infills and host sediment composition derived from LA-ICP-MS analyses. For this reason, Zn, Pb and Cr are excluded from the assessment.

4.1. SEM and high-resolution optical images

High-resolution optical images made it possible to assess sediment architecture, sediment disturbances and *Chondrites* infills at sub-mm and in natural colors, while SEM images allowed one to see compositional changes and sediment architecture, texture and distribution at higher resolution (Figs. 3–5). In most samples, *Chondrites* are easily recognized as white subcircular branches between ~0.5 and 1 mm thick. However, in some samples, *Chondrites* infills appear to be altered by the presence

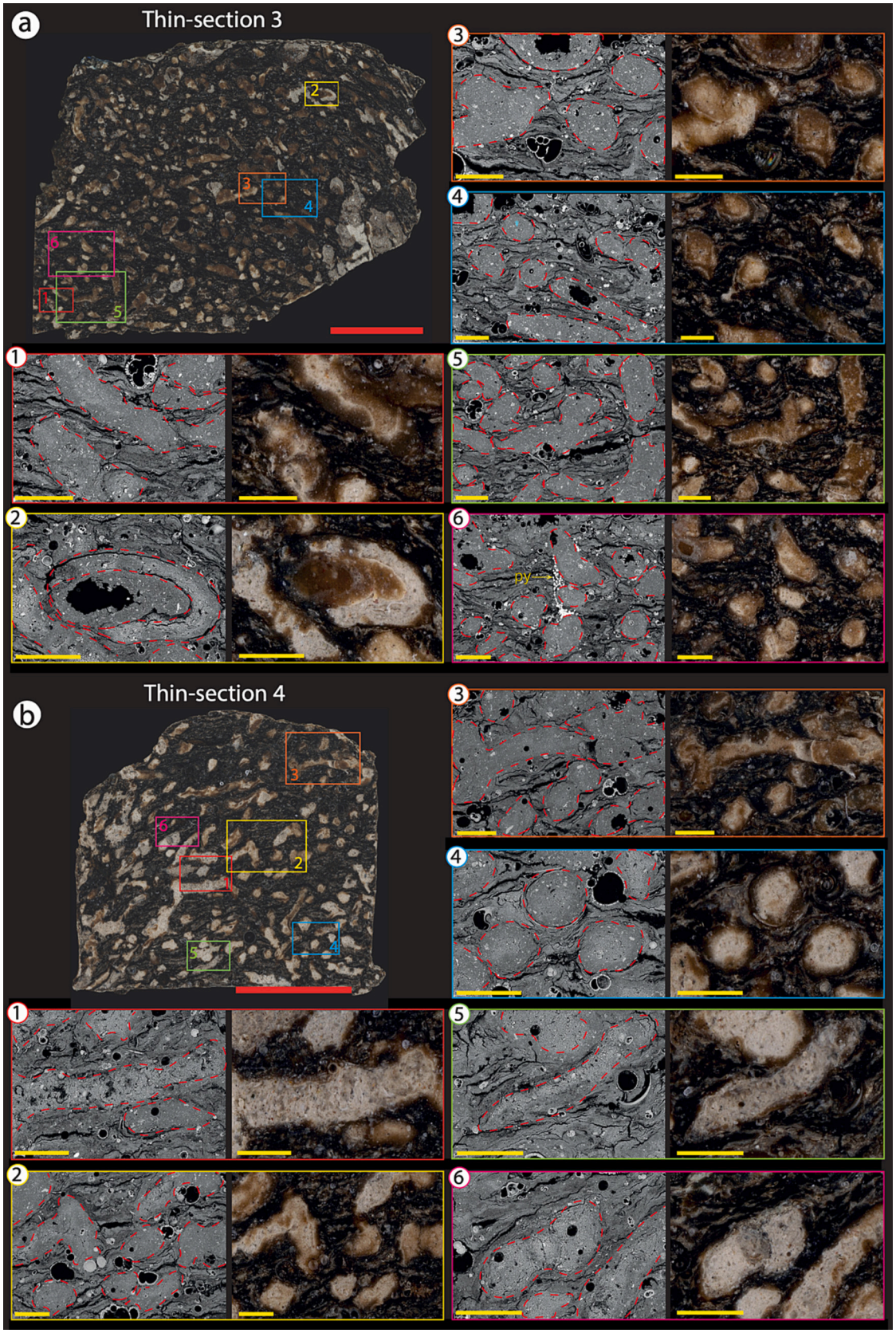

Fig. 4. High-resolution optical images of thin-sections 3 and 4, plus SEM images of selected areas (1–6). Red scale-bar: 5 mm; yellow scale-bar: 0.5 mm (500 μm). The amplified sections are shown as rectangles, each assigned a different color: (1) red, (2) yellow, (3) orange, (4) blue, (5) green, (6) magenta. White *Chondrites* are outlined with red dashed lines. (For interpretation of the references to color in this figure legend, the reader is referred to the web version of this article.)

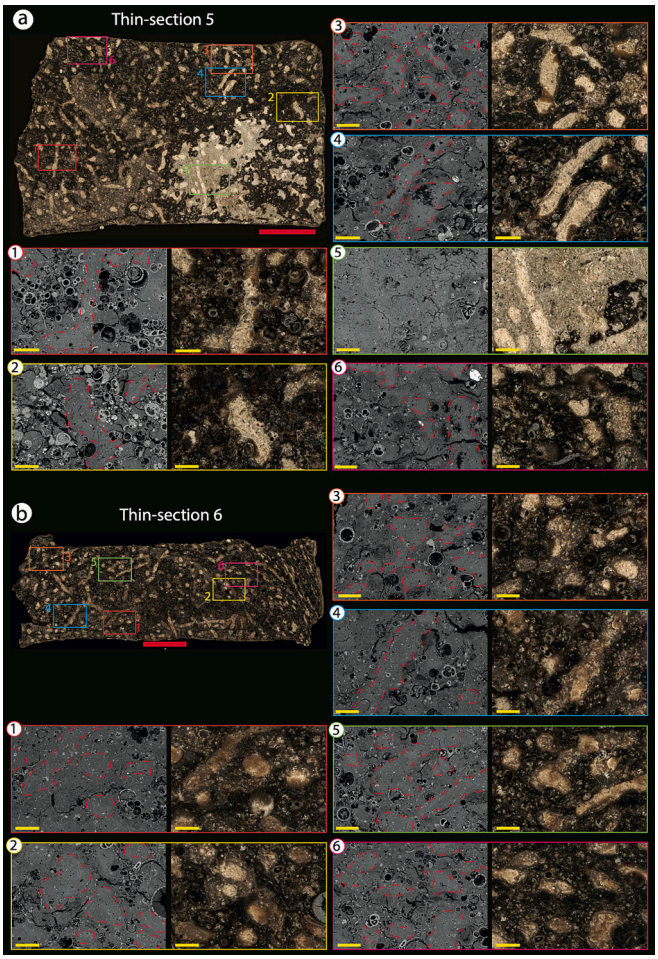

Fig. 5. High-resolution optical images of thin-sections 5 and 6, plus SEM images of selected areas. Red scale-bar: 5 mm; yellow scale-bar: 0.5 mm (500 μm). The amplified sections are shown as rectangles, each assigned a different color: (1) red, (2) yellow, (3) orange, (4) blue, (5) green, (6) magenta. White *Chondrites* are outlined with red dashed lines. (For interpretation of the references to color in this figure legend, the reader is referred to the web version of this article.)

of orange and brown haloes, as occurs in thin-sections 3, 4, 6 and 7. SEM images revealed a disturbance of *Chondrites* on sediment architecture in S7, specifically in the destruction of the syndepositional pseudolamination. In thin-section 1, situated at the top of S7, the host sediment is mixed/homogenized; therefore, it does not exhibit lamination and *Chondrites* are less evident and abundant than in the other samples. The host sediment in thin-section 1 is primarily composed of pyrite framboids with diameters >10 μm (many infilling foraminifera chambers; Figs. 3a). In thin-section 2, both optical and SEM images showed the presence of two types of *Chondrites*, with white infill and with dark brown infill, smaller in size (< 0.5 mm) (Fig. 3b). The white *Chondrites* were observed in the rest of the thin-sections, although dark brown *Chondrites* appeared to be predominantly present in this particular sample. SEM images suggest that dark brown *Chondrites* also disrupt the original syndepositional architecture of S7 sediments (Fig. 3b), but have composition a more similar to the host sediment than the white *Chondrites*, as the infilling material of these dark brown *Chondrites* has a color resembling that of the host sediment.

In thin-section 3 (Fig. 4a), *Chondrites* displayed the most intense color alteration, having marked orange and brown shades and haloes. Interestingly, in this sample, some pyrite framboids clustered around *Chondrites*. In thin-section 4, *Chondrites* coloration is less altered, yet some orange haloes are still visible (Fig. 4b). Contrasting with section S7b, section S7a (i.e., lower S7 section), lacks pseudolamination in the host sediment and exhibits lighter color, likely owing to the lower TOC content (Figs. 5 and 6). The background sediments present a "mottled" texture upon which the white *Chondrites* are superimposed. In terms of texture, however, the background sediments of S7a section are similar to the *Chondrites* infills. White *Chondrites* in section S7a are similar in size, shape and color to the *Chondrites* from section S7b. In thin-section 5, light gray sediment patches can be observed, on which the white *Chondrites* are superimposed (Fig. 5a). In thin-sections 6, 7 and 8, the white *Chondrites* also present orange haloes at the borders (Figs. 5b and 6).

4.2. EDX mapping

SEM-EDX compositional maps reveal how the disturbance of *Chondrites* affects the distribution of major elements and minerals of S7 sediments at a sub-mm scale. The white *Chondrites* in all thin-sections are similar in terms of major element composition, suggesting a similar source for the infilling sediments. The infilling material of these white *Chondrites* furthermore exhibit a homogeneous mixture of grains and minerals. In general, the respective infilling material has larger grain size, abundant angular quartz grains and a higher proportion of Ca-rich minerals in comparison to the host sediments (Figs. 7 and 8). Althought pyrite framboids are absent in *Chondrites* infill, they are present (in some cases abundant) in the host sediment (thin-section 1 and 3; Fig. 7).

Certain differences between thin-sections can be underlined here. In thin-section 1, *Chondrites* are more difficult to distinguish since the *Chondrites* infill has a composition of major elements similar to the host sediment. The dark *Chondrites* in thin-section 2 likewise exhibit a composition of major elements similar to the host sediment (Fig. 7). Therefore, they are not easily distinguished in SEM-EDX compositional maps. Still, it is evident that they disrupt host sediments and have marked contours. In thin-sections from section S7b, *Chondrites* destroy/break up the syndepositional pseudolamination within the host sediment and modify the syndepositional mineral and OM distribution (Fig. 8). The orange shades observed in the high-resolution optical images of *Chondrites* infills, especially in thin-section 3 and 4, are not reflected in compositional maps of major elements (Fig. 7). As shown by the high-resolution optical images, in thin-sections from section S7a, the host sediments do not present sub-mm lamination. *Chondrites* in section S7a have a composition, in terms of major elements, resembling *Chondrites* in section S7b (Fig. 8).

4.3. Bioturbation quantification

Following the methodology described by Dorador et al. (2014a), the high-resolution optical images of thin-sections were processed, and *Chondrites* could be highlighted and isolated (Fig. 9). Subsequently, the percentage of bioturbation was calculated based on the area (i.e. number of pixels) of these selected *Chondrites* (Fig. 9). In thin-section 1 (S7 top), the selection of *Chondrites* was difficult due to significant sediment mixing. Thus, only well-defined *Chondrites* were chosen for bioturbation quantification in this sample, which probably determined the low bioturbation recorded. In the rest of thin-sections, *Chondrites* were well identified and selected for bioturbation quantification. In thin-section 2, the two types of *Chondrites* were selected and quantified independently (Fig. 9). The dark brown *Chondrites* constitute only 4% and are only recognized in a 0.5 cm thick interval, while the white *Chondrites* represent 28%. Hence the total bioturbation percentage in this sample is 32% (Fig. 9). This finding is in accordance with thin-sections 3, 4, 7 and 8, where white *Chondrites* range between 34 and 36% (Fig. 9). In thin-sections 5 and 6, the bioturbation percentage attributed to *Chondrites* was lower, respectively ranging from 21% to 26% (Fig. 9). In thin-section 5, the presence of white sediment patches hindered *Chondrites* identification and differentiation from the host sediment (Fig. 9). It

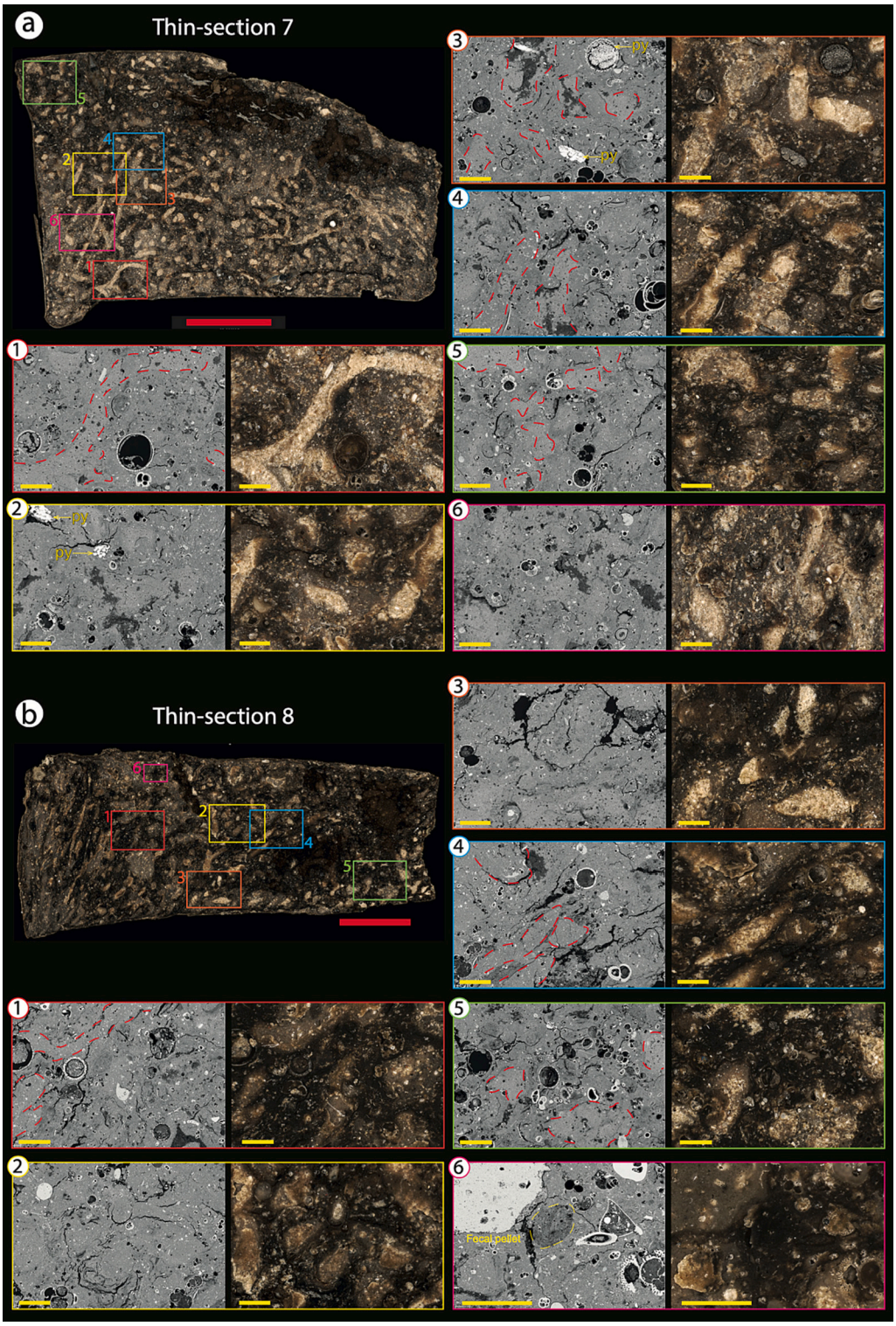

Fig. 6. High-resolution optical images of thin-sections 7 and 8, plus SEM images of selected areas. Red scale-bar: 5 mm; yellow scale-bar: 0.5 mm (500 μm). The amplified sections are shown as rectangles, each assigned a different color: (1) red, (2) yellow, (3) orange, (4) blue, (5) green, (6) magenta. White *Chondrites* are outlined with red dashed lines. (For interpretation of the references to color in this figure legend, the reader is referred to the web version of this article.)

should be noted that variations in resin impregnation in thin-sections 6, 7, and 8 resulted in differences in surface brightness and color, impeding the automated selection of *Chondrites* (Fig. 9). In these areas, the identification and isolation of *Chondrites* had to be done manually. However, the *Chondrites* infill area (i.e. the number of pixels) selected manually is comparable to the *Chondrites* infill area that would have been selected automatically.

4.4. LA-ICP-MS spot-analyses

LA-ICP-MS spot-analyses were conducted on thin-sections to compare trace metal concentrations between *Chondrites* infills and host sediment. As previously stated, this comparison will focus exclusively on trace metals that exhibit a significant enrichment in the authigenic fraction and a weak influence from the detritic fraction (i.e. V, Co, Ni,

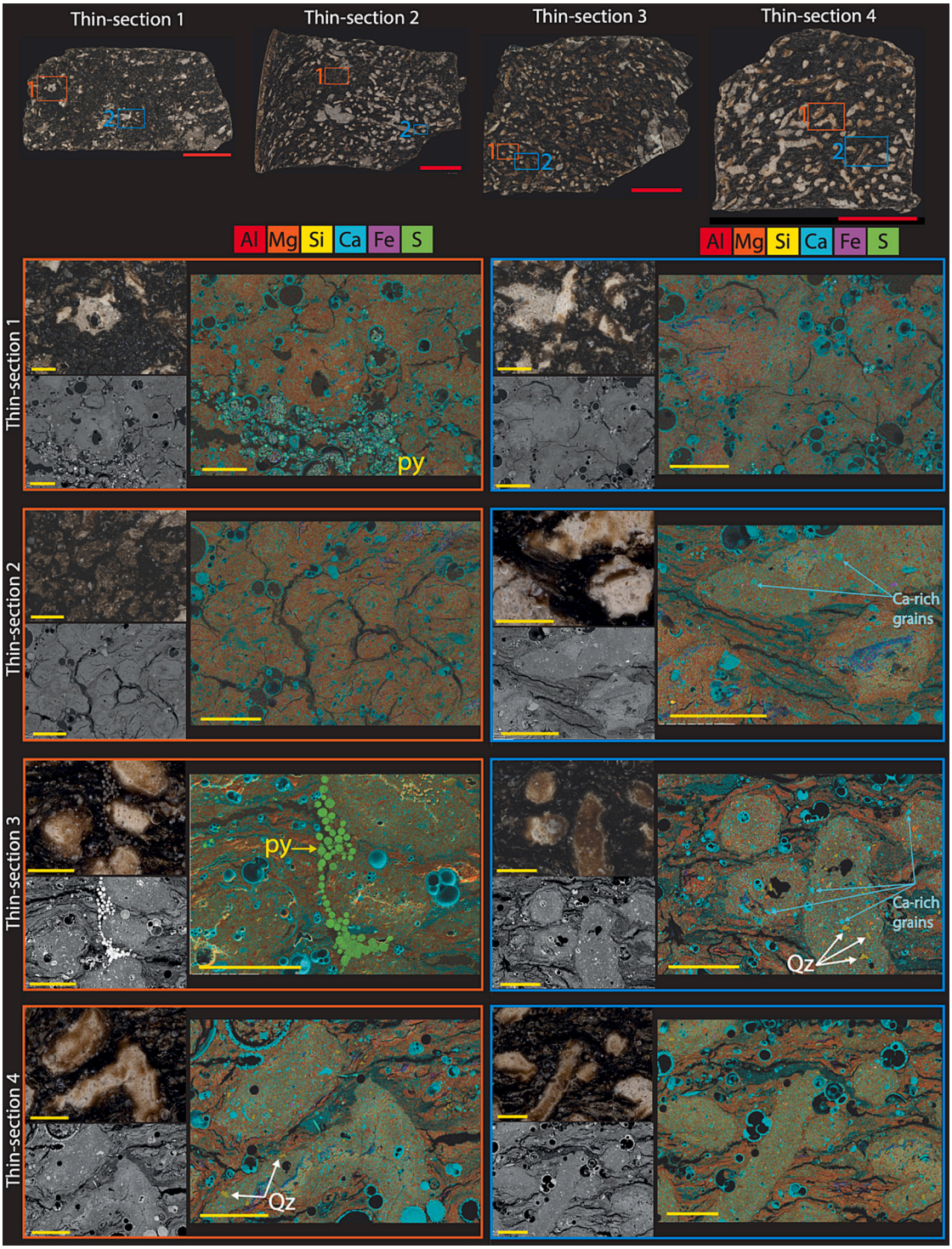

Fig. 7. Selected SEM-EDX compositional maps of major elements of selected areas on thin sections 1, 2,3 and 4 from section S7b. Mapped major elements: Al: red; Si: yellow; Mg: orange; Ca: blue; S: green and Fe: magenta. Red scale-bar: 5 mm; yellow scale-bar: 0.5 mm (500 μm). Qz: quartz grains, py: pyrite framboids. See Fig. S9 in Sup. Mat. for additional SEM-EDX compositional maps of thin-sections 2 and 4. (For interpretation of the references to color in this figure legend, the reader is referred to the web version of this article.)

Cu, Mo, Ba and U), as confirmed by the PCA (Fig. 2d). Among all thin-sections, thin-section 1 exhibits the lowest trace metals concentrations (Fig. 10b). Most trace metals (V, Co, Ni, Cu and U) have slightly higher concentrations in the host sediment than in the *Chondrites* infills, while Mo and Ba have similar values in both sediment fractions (Fig. 10). In thin-section 2, dark *Chondrites* show similar or higher trace metal concentrations than the host sediment, whereas white *Chondrites* show lower trace metal concentrations than the host sediment. Overall, thin-section 2 has the highest trace metals concentrations in the host sediment (Fig. 10). In thin-section 3, where *Chondrites* appear more altered by the presence of orange shades, no significant differences exist in trace metals concentrations between the *Chondrites* infills and host sediment.

Interestingly, Cu and Ni have significantly higher concentrations in *Chondrites* infills than in the host sediment, while V, Co, Mo, Ba and U

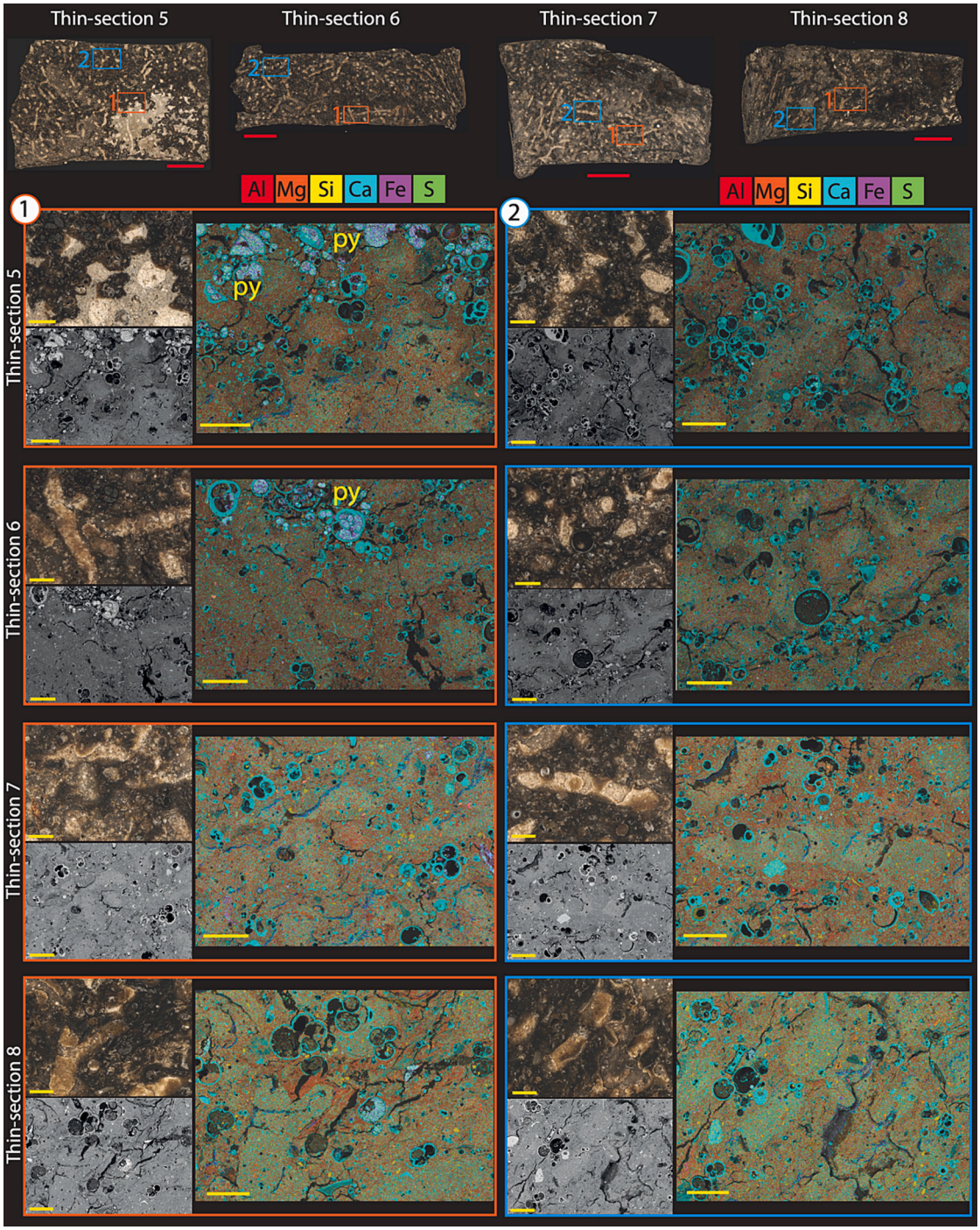

Fig. 8. Selected SEM-EDX compositional maps of major elements of selected areas on thin sections 5, 6,7 and 8 from section S7a. Mapped major elements: Al: red; Si: yellow; Mg: orange; Ca: blue; S: green and Fe: magenta. Red scale-bar: 5 mm; yellow scale-bar: 0.5 mm (500 μm). See Figs. S9 and S10 in Sup. Mat. for additional SEM-EDX compositional maps of thin-sections 5–8. (For interpretation of the references to color in this figure legend, the reader is referred to the web version of this article.)

have similar concentrations in both sediment fractions (Fig. 10). In thin-section 4, all trace metals exhibit higher concentrations in the host sediment than *Chondrites* infills, yet these differences are less marked for Co, Mo and U. In section S7a (thin-sections 5, 6, 7 and 8), trace metal concentrations in host-sediments and *Chondrites*-infills are systematically lower than in thin-sections from section S7b (Fig. 11). This could be expected, since the bulk sediments analyses of section S7a, showed that trace metal concentrations and TOC content were significantly lower than in section S7b (Fig. 2). Still, the tendency of higher concentrations of trace metals in the host-sediment than in *Chondrites*-infills is maintained, and in some cases, proportionally higher than in section S7b –as occurs with Ba, Cu and Ni (Fig. 11 and Table 2).

5. Discussion. *Chondrites* and micro-scale sediment disturbances

Bioturbation can disrupt sediment layers and mix different materials within the sediment from macro- to a microscale (Bromley, 1996). *Chondrites*, being small traces relatively common in organic-rich sediments, may disrupt sedimentary architecture at the sub-cm scale, and thereby, affect the distribution of trace metals (including diagnostic

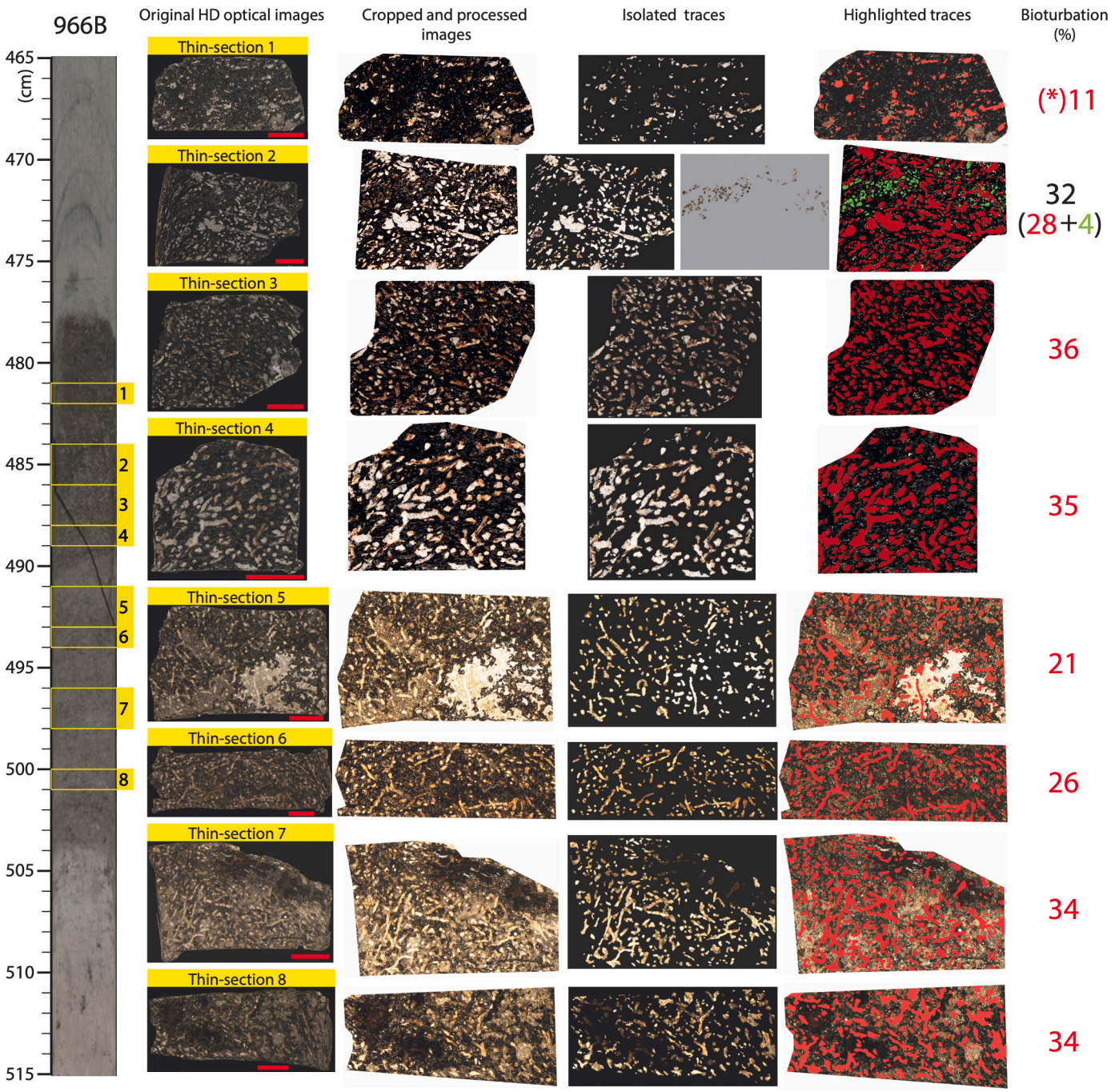

Fig. 9. Image treatment and bioturbation quantification using Photoshop CS6 methodology developed by Dorador et al., 2014a, 2014b. Bioturbation index is indicated for each thin-section. Core image shown on the left to indicates the depth of each thin-section. Red scale-bar: 5 mm. (*) Bioturbation (%) obtained from quantification of irregular white *Chondrites* in thin-section 1 characterized by strong sediment mixing. (For interpretation of the references to color in this figure legend, the reader is referred to the web version of this article.)

RSTMs and oligoelements) and OM within the sediments (Löwemark et al., 2006; Baucon et al., 2020).

5.1. *Chondrites*: lamination, texture and mineral composition

In S7 sediments at the top of Eratosthenes Seamount, *Chondrites*-producers bioturbated from 11% to 36% of the total volume of organic-rich sediments. Thus, despite its small size, the high abundance has a strong impact on the small-scale lamination, texture, and minerals, and OM distribution of the organic-rich sediments. A high abundance of *Chondrites* can produce disruption, or even destruction of sub-mm lamination or pseudolamination, which can serve as high-resolution paleoenvironmental archives (Jilbert et al., 2008, 2010; Hennekam et al., 2015; Sosa-Montes de Oca et al., 2018). Sediment bioturbation by *Chondrites*-producers can therefore alter valuable geochemical information used to reconstruct past redox conditions at high-temporal resolution (Figs. 10 and 11).

Micro-scale disturbances can be recognized by the mineral distribution. The assessed white *Chondrites* infills exhibit a high abundance of angular quartz grains (typically associated with aeolian input) and Ca-enriched material, along with much lower TOC content than the host sediment, according to color contrast. Meanwhile, the host sediment is

ⓐ

Section S7b	Median values (μ g/g)	V	Co	Ni	Cu	Mo	Ba	U
	Thin-section 1 (B%=11)							
	Host Sediment (n =41)	101	58	78	32	2	189	3
	Chondrites infill (n =76)	83	12	68	18	2	190	1
	Thin-section 2 (B%=28)							
	Host Sediment (n =23)	541	84	321	290	67	900	21
	White Chondrites infill (n =58)	460	77	269	228	51	782	18
	Dark *Chondrites* infill (n =12)	628	97	379	271	89	909	25
	Thin-section 3 (B%=36)							
	Host Sediment (n =20)	403	67	216	154	32	493	14
	Chondrites infill (n =51)	404	69	227	165	30	497	15
	Thin-section 4 (B%=35)							
	Host Sediment (n =44)	417	69	238	218	21	520	17
	Chondrites infill (n =100)	365	63	208	180	17	478	14

ⓑ

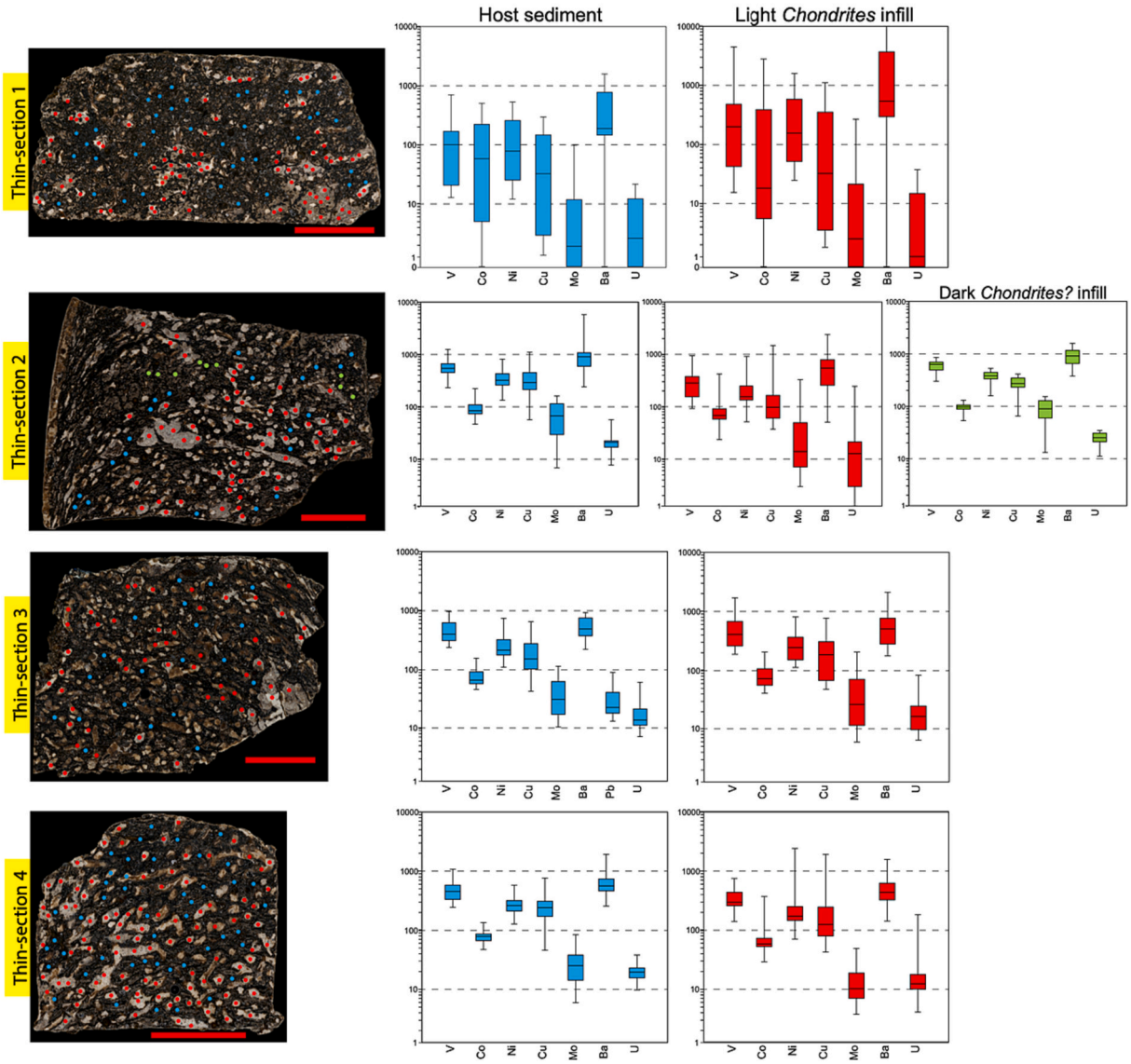

Fig. 10. Box-plots of LA-ICP-MS spot-analysis results on thin-sections 1, 2, 3 and 4 from section S7b. (a) Table of TMs concentrations (μg/g) obtained by LA-ICP-MS spot-analyses in the host sediment and *Chondrites* infills. n = number of spot-analyses. (b) Box-plots of LA-ICP-MS spot-analyses results. The high-resolution optical images are indicated the locations of the LA-ICP-MS spot-analysis. Blue dots: host-sediment; red dots: *Chondrites* infills. Accordingly, blue box-plots indicate host-sediment results, while red box-plots indicate *Chondrites* infill results. LA-ICP-MS results of the dark Chondrites observed in thin-section 2 are shown in green. Red scale-bar: 5 mm. All box-plots have $\log_{10}$ scale. (For interpretation of the references to color in this figure legend, the reader is referred to the web version of this article.)

more enriched in OM and clay minerals enriched in Al, Mg and K (typically linked to fluvial input) (Figs. 7 and 8). In this context, *Chondrites*-producers introduced overlying sediments, deposited during dryer climatic conditions and lower export productivity, into the S7 sediments deposited during high fluvial inputs. This resulted in alterations in mineral distribution at the sub-cm scale and a reduction in the overall TOC content (Figs. 7 and 8), given that the sediments overlying S7 have an average lower TOC (~ 0.5%; Table S3 in Sup. Mat.) and the light

ⓐ

	Median values (μ g/g)	V	Co	Ni	Cu	Mo	Ba	U
Section S7a	**Thin-section 5 (B%=21)**							
	Host Sediment (n =23)	268	50	172	174	8	376	15
	Chondrites infill (n =54)	184	37	122	75	3	233	8
	Thin-section 6 (B%=26)							
	Host Sediment (n =26)	193	49	173	151	4	544	12
	Chondrites infill (n =50)	182	44	138	79	4	335	9
	Thin-section 7 (B%=34)							
	Host Sediment (n =22)	220	48	173	151	7	393	11
	Chondrites infill (n =55)	156	35	112	71	3	232	7
	Thin-section 8 (B%=34)							
	Host Sediment (n =23)	261	51	161	146	6	402	10
	Chondrites infill (n =34)	219	47	144	86	4	355	8

ⓑ

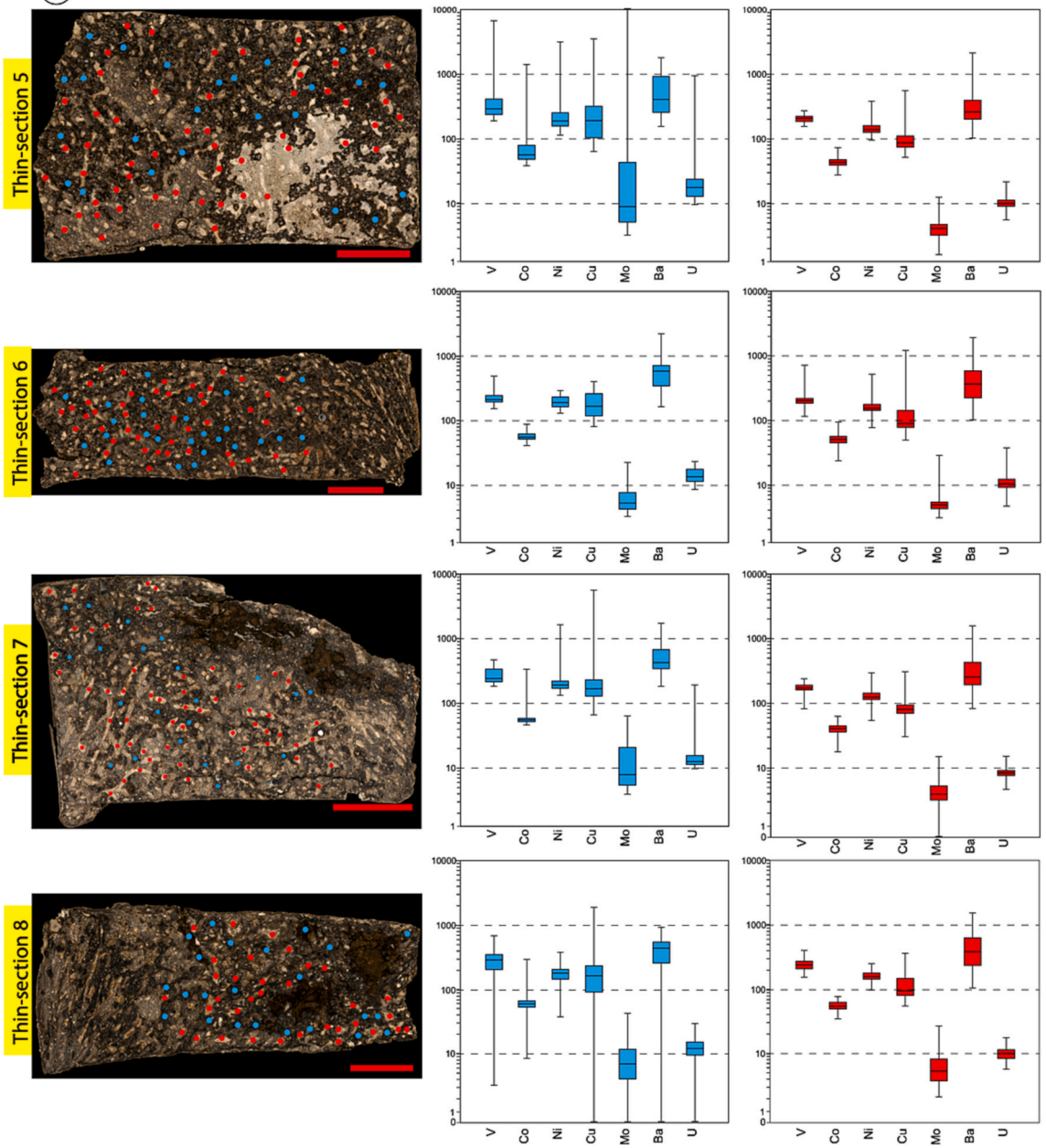

Fig. 11. Box-plots of LA-ICP-MS spot-analysis results of thin-sections 5, 6, 7 and 8 from section S7a. (a) Table of TMs concentrations ($\mu g/g$) obtained by LA-ICP-MS spot-analyses in the host sediment and *Chondrites* infills. n = number of spot-analyses. (b) Box-plots of LA-ICP-MS spot-analysis results. The high-resolution optical images are indicated the locations of the LA-ICP-MS spot-analyses. Blue dots: host-sediment; red dots: *Chondrites* infill. Accordingly, blue box-plots indicate host-sediment results, while red box-plots indicate *Chondrites* infills results. Red scale-bar: 5 mm. All box-plots have $\log_{10}$ scale. (For interpretation of the references to color in this figure legend, the reader is referred to the web version of this article.)

Table 2
Calculated weighted average TM concentration [wTM] and dilution factor (df). Mean and maximum dilution factor values are indicated at the bottom for each TM. $[TM]_{hs}$ = median TM in the host sediment.

		LA-ICP-MS ($\mu g/g$)						
		V	Co	Ni	Cu	Mo	Ba	U
S7b section	**Thin-section 1**							
	[TM]hs	101	58	78	32	2	189	3
	[wTM]	99	53	77	31	2	189	2
	df (%)	2	9	1	5	-2	0	6
	Thin-section 2							
	[TM]hs	541	84	321	290	67	900	21
	[wTM]	522	83	309	272	64	867	20
	df (%)	4	2	4	6	5	4	3
	Thin-section 3							
	[TM]hs	403	67	216	154	32	493	14
	[wTM]	404	68	220	158	31	494	14
	df (%)	0	-1	-2	-3	2	0	-2
S7a section	**Thin-section 4**							
	[TM]hs	417	69	238	218	21	520	17
	[wTM]	399	67	228	205	20	505	16
	df (%)	4	3	4	6	7	3	5
	Thin-section 5							
	[TM]hs	268	50	172	174	8	376	15
	[wTM]	250	47	161	153	7	346	14
	df (%)	7	6	6	12	12	8	10
	Thin-section 6							
	[TM]hs	193	49	173	151	4	544	12
	[wTM]	190	48	164	132	4	490	11
	df (%)	1	3	5	12	3	10	6
	Thin-section 7							
	[TM]hs	220	48	173	151	7	393	11
	[wTM]	198	44	152	124	5	338	9
	df (%)	10	9	12	18	17	14	11
	Thin-section 8							
	[TM]hs	261	51	161	146	6	402	10
	[wTM]	247	50	155	126	5	386	9
	df (%)	5	3	4	14	8	4	5

	V	Co	Ni	Cu	Mo	Ba	U
Median df (%)	4	4	4	9	7	5	6
Maximum df (%)	10	9	12	18	17	14	11

color of the white *Chondrites* infills indicates minimal organic carbon content.

OM and pyrite framboids are not equally distributed between *Chondrites* infills and the host sediment. Pyrite framboids and OM are present in the host sediment but absent in white *Chondrites* (Figs. 3 to 8). The connection to overlying oxic waters through *Chondrites* burrows would promote higher oxygen levels within the *Chondrites* network than in the host sediment, where dysoxic-anoxic conditions prevailed (according to the enrichment of RSTMs; Fig. 2). Nevertheless, the presence of pyrite framboids and Mo enrichments in the sediments suggest that intermittent euxinic conditions were reached in confined sub-cm microenvironments, e.g. inside foraminifera chambers (Figs. 3 to 8) (Wilkin et al., 1996, 1997; Tribovillard et al., 2008; Scott and Lyons, 2012; Lin et al., 2016; Liu et al., 2019; Chang et al., 2022; Monedero-Contreras et al., 2023b). *Chondrites*, as open, actively ventilated burrows are expected to have less abundant (or absent) pyrite than the surrounding sediment (Baucon et al., 2020). Such observations allow us to state that *Chondrites* distribution, abundance and associated irrigation exerted control on OM, S and Fe distribution and chemistry within the sediment during early diagenesis pyrite precipitation (Phillips and McIlroy, 2010). The absence of pyrite framboids in *Chondrites* infills could also be related with the ethology of the organism; *Chondrites*-producers ingested the microbially degraded OM from which framboids would have originated (Baucon et al., 2020). Furthermore, research has revealed a correlation between elevated populations of benthic fauna and an increased occurrence of pyrite precipitation within the underlying sediment. This phenomenon is attributed to the augmented influx of sulfate-rich water into the oxygen-depleted sediments, which subsequently enhances the activity of sulfate-reducing bacteria and the precipitation of pyrite framboids (Hantsoo et al., 2023). This might explain the high abundance of pyrite framboids surrounding some *Chondrites* (Fig. 7, thin-section 3). Yet, evidence from S isotopes indicates that during sapropel deposits in the Eastern Mediterranean, porewater was saturated in sulfate (Passier et al., 1996). Additional support for permanent sulfate saturation comes from the preservation of biogenic barite crystals in sapropel sediments (Martínez-Ruiz et al., 2000; Monedero-Contreras et al., 2023b). Therefore, *Chondrites*-producers would not significantly change sulfate saturation in Eastern Mediterranean porewater during sapropel termination. In deep-marine settings where sulfate is depleted in the porewater, *Chondrites*-producers would, however, bear a major impact by replenishing the depleted sulfate in the porewater.

The mixing and disturbance of sediments by benthic organisms through burrowing, feeding, and movement strategies can vary due to changes in redox conditions and OM content (Bromley and Ekdale, 1984; Bromley, 1996; Buatois and Mángano, 2016; Baucon et al., 2020). Such variations lead to differences in the degree of bioturbation and in the distribution of OM and oligoelements within the sediment. For instance, background sediments in section S7a present a different distribution of OM and sediment texture than section S7b owing to differences in bottom-water redox conditions (see section 4.3 and Fig. 13). The section S7a background sediments show a scattered distribution of OM and a mottling texture, while in section S7b the OM is concentrated within sub-mm laminae. The different modifications in sediment texture and sub-mm architecture by *Chondrites*-producers and other benthic fauna can give rise to diverse distributions of oxygen, OM, S and Fe in the sediments and porewater (Fig. 12). These differences imply a range of potential effects on nutrient cycling, sediment biogeochemistry, and overall macro to micro ecosystem dynamics. Bioturbation modelling and neoichnological studies in modern marine settings demonstrate how macrofauna (e.g. *thyasirid* burrows; Dufour and Felbeck, 2003; Dando et al., 2004) and meiofauna (e.g. nematodes; Moens et al., 2005) can enhance OM degradation, increase microbial and bacterial growth, increase solute transport and molecular diffusion, increase sulfide oxidation, shorten porewater turnover time, and alter the vertical distribution of sedimentary phosphorus (Kamp-Nielsen et al., 1982; Meadows et al., 1991; Neira et al., 2001; Löhr and Kennedy, 2015; Arndt et al., 2013; Jørgensen and Nelson, 2004; Jørgensen et al., 2022).

5.2. *Chondrites: trace elements distribution and geochemical signals*

The preservation and distribution of trace metals in organic-rich sediments are influenced by various factors that include marine productivity, redox conditions in the water-column and porewater, detrital input, chemical diagenesis, and bioturbation (Bromley, 1996; Zheng et al., 2002; Tribovillard et al., 2006; Monedero-Contreras et al., 2023b, 2024). As mentioned before, *Chondrites*-producers may bioturbated considerable volumes (up to 36%) of organic-rich S7 sediments (Fig. 9), which diluting the syndepositional concentration of trace metals, even trace oligoelements (e.g. Mo, V, Ni, Cu and Co) and TOC. The median dilution factor values of trace metals range from 4% to 9%, while the standard deviation values are from 3% to 7%. Cu and Mo exhibit the highest degree of dilution by *Chondrites*-producers, reaching up to 18% and 17%, respectively. This suggests significant variability in the dilution of different trace metals (Table 2). The variable dilution for RSTMs and Ba could be attributed to differences in the speciation and mobility of trace metals under different redox conditions (Tribovillard et al., 2006; Calvert and Pedersen, 2007). Evident dilution of trace metals concentrations supports the interpretation that *Chondrites*-producers introduce oxic/dysoxic material impoverished in RSTMs, barite and OM downward into anoxic host sediments more enriched in RSTMs, barite and OM (Fig. 12). Furthermore, as indicated above, the mixing of materials by *Chondrites* can impact trace metal speciation and mobility,

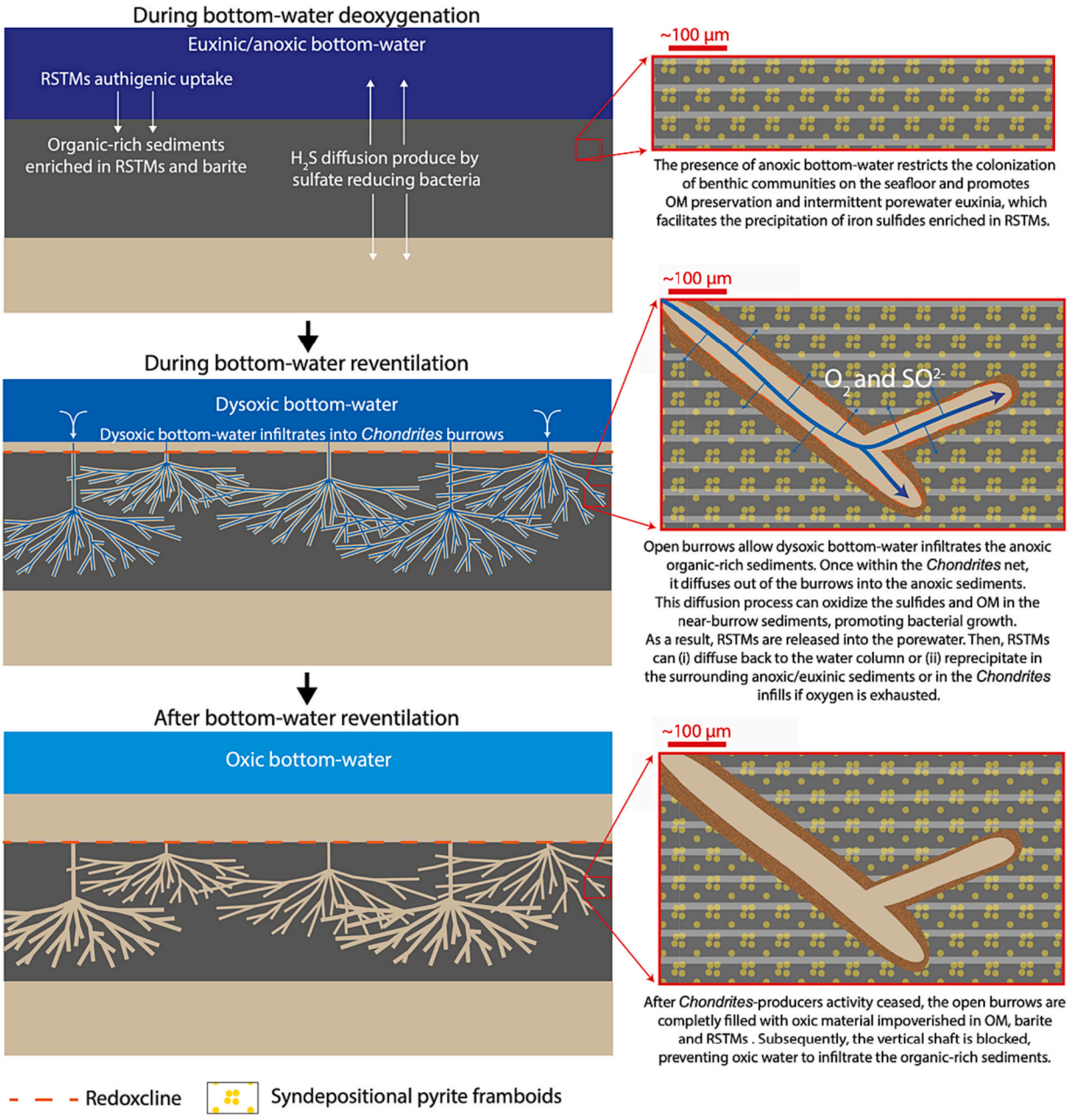

Fig. 12. *Chondrites* evolution scheme in organic-rich sediments and induced geochemical processes at sub-cm scale.

thus influencing their bioavailability, and subsequently the microbial activity, efficiency of OM degradation and nutrient cycling within the sediment (Green and Chandler, 1994; Rysgaard et al., 2000).

In thin-section 2, the dark *Chondrites* appear in a limited ~5 mm thick interval (Figs. 3 and 9). These *Chondrites* do not exhibit a strong color contrast and have a composition of major elements and trace metals similar to that observed in the host sediment (Figs. 7 and 10). One explanation for the existence of these dark *Chondrites* is bioturbation by tracemakers during deposition of the sediments overlying thin-section 2, when a slight increase in oxygen levels occurred. Vertical plots reveal an increase in oxygen levels above thin-section 2 (at 484 cm; see Fig. 2a), supported by a correlative decrease in TOC (%), DOPt values and certain Al-normalized RSTMs (e.g. Mo, U, Ni, and, to a lesser extent, Cu). In this case however, *Chondrites*-producers had to be highly resistant to low oxygen levels (slightly oxygenated during thin-section 2 deposition) because the infills reflect oxygen depleted bottom-waters and high productivity levels, as suggested by the high concentrations of RSTMs and Ba. An alternative explanation is that the infill of these *Chondrites* corresponds to fecal material introduced by active backfilling (Löhr and Kennedy, 2015); still, this possibility is controversial as such behavior has only been reported from uncertain *Chondrites* (Knaust, 2017; Baucon et al., 2020). At any rate, this hypothesis might explain the similarities in geochemical and mineral composition, as well as in texture (grain size) and color, with regard to those of the host sediment.

In thin-section 3, where *Chondrites* infills appear darkened with orange/brown shades and haloes, potentially indicating postdepositional alteration, the concentrations of trace metal are comparable to or even higher than those observed in the host sediment, with dilution factors ranging from 2% to −3% (Table 2). This could be explained by the postdepositional oxidation and remobilization of trace metals in the near-burrow sediments, and the subsequent reprecipitation within *Chondrites* infills. *Chondrites* burrows open to the sediment-water interface allowed oxic water to flow into the *Chondrites* network. Oxygenated water, whether derived from the moment of deposition of the layer

corresponding to thin-section 2 (deposited during an oxygen increase in bottom-water) or from S7 overlying sediments deposited after sapropel termination, could diffuse out of the *Chondrites* network into the anoxic sediments and create sub-mm oxic areas surrounding the burrows (Fig. 12) (Jovanovic et al., 2014). This may lead to the oxidation of host mineral phases of RSTMs in the surrounding sediments, resulting in dissolved RSTMs in the porewater that can reprecipitate within the sediment or diffuse upwards to the oxic/dysoxic bottom-water. The precipitation of RSTMs in the *Chondrites* infills could occur in association with Mn and Fe oxyhydroxides under dysoxic conditions into the

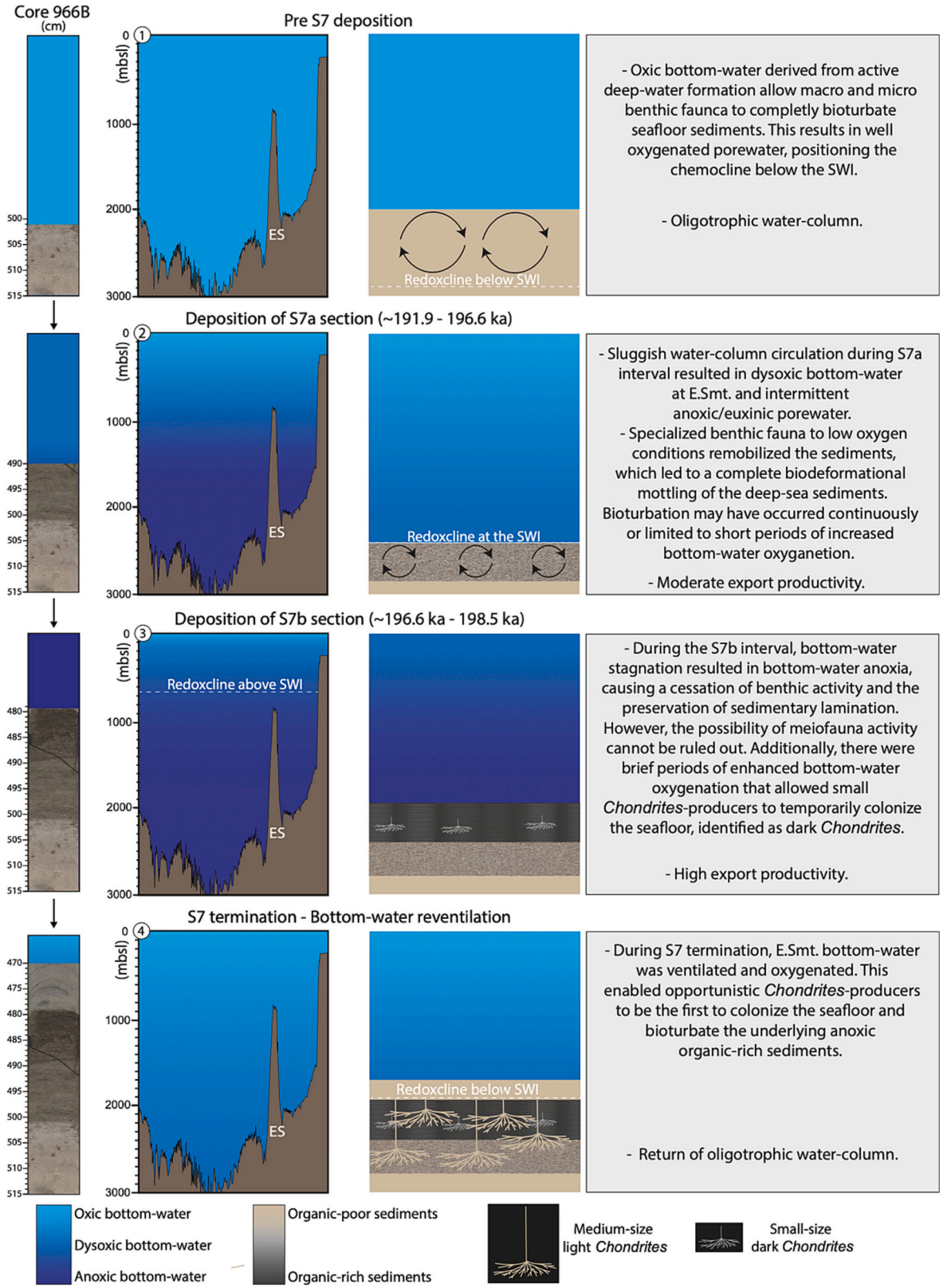

Fig. 13. Scheme of S7 evolution at Site 966B using geochemical and ichnological information. SWI: sediment-water interface; E.Smt.: Eratosthenes Seamount.

Chondrites burrows. Yet this suggestion does not fully account for U enrichments, as U tends to precipitate as uranite during anoxic conditions rather than in association with Fe or Mn oxyhydroxides under dysoxic conditions (McManus et al., 2005; Tribovillard et al., 2006; Calvert and Pedersen, 2007 and references therein). Moreover, SEM-EDX maps of altered *Chondrites* do not show Mn enrichments (Fig. 7). An alternative mechanism for the reprecipitation of RSTMs must therefore be evoked to explain such enrichments. One potential explanation is that dissolved RSTMs reprecipitated within *Chondrites* infills, probably by absorption and/or co-precipitation into authigenic phases, once oxygen was depleted again due to aerobic bacterial activity along with OM and sulfides oxidation.

In any case, *Chondrites*-producers are changing the redox conditions in confined sub-cm areas of the anoxic organic-rich sediments and the distribution of RSTMs, including some oligoelements such as Fe, S, Mo, Co, Cu, V and Ni (Fig. 12). Aller (1994) stated that cyclic redox patterns are common within individual burrow structures and are accompanied by rapid switching in dominant metabolic processes, generating geometrically and temporally complex redox mosaics in the sediment matrix. This observation aligns with findings by Jørgensen et al. (2005) and Meysman et al. (2006), who state that oxic sub-cm microniches can occur along the burrow walls in anoxic sediments due to occasional oxic ventilation. Yin et al. (2017) further corroborated this by demonstrating how burrowing ragworms (polychaete *Nereis succinea*) oxidize the walls of the burrows in salt marsh sediments. Accordingly, the irrigation by *Chondrites*-producers creates a complex sub-cm redox mosaic within the sediments and can potentially enhances microbial productivity, involving sulfur-oxidizing and magnetotactic bacteria in the near-burrow sediments where the redox transition zones are located (Lefèvre and Bazylinski, 2013).

5.3. Multiproxy reconstruction of S7 evolution

The compiled geochemical dataset and ichnological assessments of S7 enable a multiproxy paleoenvironmental reconstruction of the S7 evolution, deposited between ~198.5 and 191.9 ka (Ziegler et al., 2010). S7 was deposited during very humid conditions with large nutrient-rich fluvial inputs from the African borderlands, primarily by the Nile River (Gallego-Torres et al., 2007a, 2007b; Wu et al., 2018). Hence, the S7 sediments are enriched in OM as a result of increased export productivity and oxygen-depleted bottom-waters (Benkovitz et al., 2020; Sweere et al., 2021). As previously stated, the S7 event at the Eratosthenes Seamount can be divided in to two sub-sections tied to different redox and environmental conditions (Fig. 2a). The deposition of section S7a (from 503.5 to 491 cm of core 966B; Fig. 2) was accompanied by a moderate increase in productivity and weak deep-water restriction due to intermittent bottom-water ventilation/oxygenation, followed by low RSTMs authigenic enrichment. During the S7a period, oxic to dysoxic conditions most likely prevailed at the top of Eratosthenes Seamount. They allowed macro and micro-opportunistic organisms to intermittently colonize the seafloor and homogenize the sediments, erasing sub-mm lamination and producing a mottled texture (Fig. 13) (Rodríguez-Tovar, 2022). Further evidence of syndepositional benthic activity lies in the presence of fecal pellets (see thin-section 8 in Fig. 6b.6) (Löhr and Kennedy, 2015). In this framework, OM accumulation/preservation was not very efficient during S7a period; TOC content does not exceed 2%, supporting a weak oxygen-depletion at this water-depth in conjunction with moderate productivity (Fig. 2). Nevertheless, intermittent and confined porewater euxinia must be evoked to explain the Mo enrichments and the presence of euhedral pyrite framboids in the host sediments of section S7a (Helz et al., 1996; Tribovillard et al., 2008; Scott and Lyons, 2012; Helz and Vorlicek, 2019).

The mixing and biodeformation of the sediments during period S7a probably took place through the interplay of two different bioturbational mechanisms, creating a distinctive "mottled" sediment texture (Fig. 13): (i) in fine sediments with high water content, burrows created by macrotracemakers appear as biodeformational sedimentary structures, showing no distinct outline, leading to total sediment mixing without evident signs of well-defined burrows, outlines, or color contrasts (Rodríguez-Tovar, 2022), and (ii) meiofauna, despite their small size, could have actively mixed and homogenized the sediments. Furthermore, the bioturbation might have been a continuous process throughout S7a deposition, or else could have been limited to periods of increased bottom-water oxygenation. The grayish sediment patch in thin-section 5 (Fig. 5) appears to be syndepositional because the presence of *Chondrites* "cuts" through it, and the irregular outline suggests it is not a biosedimentary structure. It can thus be interpreted as a partially erased oxic layer with low TOC (due to bioturbation) that was deposited during bottom-water ventilation. Even though brief bottom-water ventilations might have occurred, no apparent indications are seen in the geochemical record (e.g. Mn peak; Fig. 2) (Filippidi and de Lange, 2019; Monedero-Contreras et al., 2023b). Still, we cannot be discarded the possibility that Mn-oxyhydroxides precipitating during ventilation might have undergone postdepositional dissolution as a result of the redox transition towards anoxic porewaters during the deposition of S7b section.

If a near-constant sedimentation rate is assumed for the entire S7 event −considering Ba enrichment as the complete sapropel event following Gallego-Torres et al. (2010) methodology− one may surmise that a change in water-column dynamics, redox conditions, and productivity rate occurred around 196.6 ka at the top of the Eratosthenes Seamount. This change marked the onset of the S7b period, characterized by (i) stronger deep-water stagnation, which boosted bottom-water deoxygenation at the top of Eratosthenes Seamount and enhanced adsorption and/or co-precipitation of RSTMs into authigenic phases by seafloor sediments, and (ii) increased productivity, that enhancing barite precipitation in the water-column (Fig. 13). The accumulation/preservation of OM was thereby enhanced, which derived in higher TOC content in S7b section (TOC up to 3.4%; Fig. 2a). Higher Mo concentrations and the high abundance of pyrite nanocrystals (> 1 μm) in the host sediments further supports that euxinic conditions may have been reached not only within confined microenvironments in the porewater-sediment system, but also sporadically in bottom-waters at the top of Eratosthenes Seamount (Wilkin et al., 1996, 1997; Wilkin and Barnes, 1997; Scott and Lyons, 2012; Lin et al., 2016; Liu et al., 2019; Chang et al., 2022). The existence of sub-mm lamination furthermore indicates that macro benthic organisms were absent from ~196.6 ka to 191.9 ka because of bottom-water anoxia (Fig. 13). The existence of meiofauna that living between the grains, incapable of disturbing sub-mm lamination, cannot be ruled out, however (Löhr and Kennedy, 2015). Such insights would indicate that during period S7b the redoxcline in the Eastern Mediterranean was placed above ~900mbsl due to strong water-column stratification and deep-water deoxygenation (Benkovitz et al., 2020; Sweere et al., 2021; Monedero-Contreras et al., 2023a, 2024). A correlative decrease in various RSTMs concentrations at 484 cm deep points to a brief period of weakened bottom-water anoxia around 194–193 ka at Eratosthenes Seamount. This allowed small *Chondrites* tracemakers to colonize the seafloor for a short spell, until bottom-water anoxia returned (Fig. 13); hence small dark *Chondrites* in the underlying sediment present a very similar composition to the host sediment and are only observed within a 0.5 cm thick interval (thin-section 2; see Figs. 3 and 9).

After S7s termination, dryer conditions ruled in the Eastern Mediterranean, meaning decreased fluvial input, increased aeolian influence, and lower OM accumulation/preservation. The end of S7 at Eratosthenes Seamount took place when deep-water formation/circulation was reactivated. The absence of a "marker bed" – an interval enriched in Mn-oxyhydroxides atop the S7 organic-rich sediments− does not support the occurrence of an abrupt reventilation during S7 termination at the Seamount (Wilson et al., 1986; Calvert and Pedersen, 1993; de Lange et al., 2008; Filippidi and de Lange, 2019). However, the immediate

return of oxic bottom-waters after S7s termination at the Eratosthenes Seamount is corroborated by the rapid colonization of the seafloor by opportunistic *Chondrites*-producers and by the synchronous drop in TOC, RSTMs and pyrite content at the top of S7 sediments. Since there are no signs of postdepositional sapropel burndown, e.g. a mismatch between Ba/Al and TOC (Fig. 2a) (van Santvoort et al., 1997; Monedero-Contreras et al., 2023b), we can affirm that the redoxcline was never situated below the upper boundary of the organic-rich sediments during the deposition of section S7b (Fig. 13). Despite the fact that porewater anoxia was maintained during S7 termination, *Chondrites*-producers were able to bioturbate the organic-rich sediments, taking advantage of the oxygen from the overlying oxic/dysoxic bottom-waters due to the presence of a vertical shaft.

The DOPt increases below S7 organic-rich sediments is indicative of authigenic pyrite enrichments, linked to the existence of a synsapropel interval, which corresponds to an interval with low TOC content but high pyrite content below a sapropel (Passier et al., 1996, 1997, 1999; Benkovitz et al., 2020; Matthews et al., 2017; Filippidi and de Lange, 2019; Monedero-Contreras et al., 2023b). The DOPt increase at the top of S7 corresponds to the synsapropel interval of the overlying sapropel (i.e. S6) (Monedero-Contreras et al., 2024). The precipitation of pyrite below some sapropels is controlled by the reaction of downward HS^- fluxes in contact with the upward diffusing Fe from underlying sediments (Passier et al., 1996). Thus, during S7 deposition, a downward diffusion of excess HS^- produced by sulfate-reducing bacteria promoted pyrite formation through sulfidisation of the sediments below S7 (Passier et al., 1996). This scenario implies that reactive Fe for pyrite precipitation was depleted in the organic-rich S7 sediments. Moreover, the vertical plots indicate that Co, Ni, and Cu, precipitated in association with the synsapropel pyrite (Monedero-Contreras et al., 2023b, 2024) (see Fig. 2d).

6. Conclusions

Detailed ichnological analysis reveals the influence of *Chondrites* on the RSTMs enriched in sapropel S7 (~195 ka), at the Eratosthenes Seamount (Levantine Basin, Eastern Mediterranean). *Chondrites* alter sedimentary features at a sub-cm scale, impacting lamination, texture and mineral distribution. The bioturbation of materials by *Chondrites*-producers also modifies the distribution and concentration of OM and trace elements, including oligoelements that are vital for macro and microorganisms (e.g. Fe, S, Mo, Co, Cu, V and Ni).

Chondrites-producers are able to bioturbate significant volumes of organic-rich sediments (from 11% to 35%). They can introduce overlying oxic/dysoxic material of low trace metals concentrations and OM content downward, into anoxic sediments more enriched in trace metals and OM. By doing this they can introduce oxic porewater below the sedimentary redoxcline. The whole of this process modifies redox conditions in the zones surrounding the *Chondrite*s burrows and remobilizes trace metals through the oxidation of sulfides and OM in the near-burrow sediments. Remobilized trace metals can reprecipitate within the sediment, or diffuse to bottom-waters. As a consequence, the change in trace metal speciation, mobility, and distribution influences the bioavailability of trace metals. In turn, *Chondrites* can impact carbon and nutrients cycling, microbial activity, and OM degradation, impacting in turn the overall sedimentary biogeochemistry of deep-marine sediments, where *Chondrites* tend to be abundant.

With respect to the implications for paleoceanographic/paleoenvironmental reconstructions based on geochemical signals, *Chondrites* bioturbation would dilute the overall TOC content and the concentration of paleoenvironmental diagnostic trace metals (e.g. Mo, U, V, Ba) in bulk sediment samples. Although the average dilution factor is between 5% and 6%, in some cases the dilution can be >10% for key paleoceanographic trace metals (e.g. Mo, U and Ni); depending on the abundance, distribution and infilling material composition of *Chondrites*, and on the speciation and mobility of the trace metal under different redox conditions. If the distribution of *Chondrites* remains relatively constant throughout the sampled organic-rich section, vertical trends of RSTMs will not be substantially affected. At any rate, however, *Chondrites* presence must be considered for accurate sedimentary record comparisons and for calculating trace metals and OM burial fluxes. High-resolution redox reconstructions based on sub-cm analyses (e.g. LA-ICP-MS line-scanning and XRF core-scanning) should take into account the presence of *Chondrites*, as RSTMs variations might not be related to time variations but rather to *Chondrites* infills geochemical composition.

Based on the obtained geochemical data and ichnological information, the paleoenvironmental evolution of S7 was interpreted, leading us to characterize of two phases with different redox and environmental conditions. During the lower half of S7 (S7a), deep-water stagnation and deoxygenation was weak and marine productivity was low, then, as the upper S7 section (S7b) was deposited, deep-water stagnation strengthened and marine productivity increased. This enhanced deep-water deoxygenation, OM accumulation/preservation and trace metal authigenic uptake, in addition to shallowing the redoxcline above 900 mbsl and inhibiting the establishment of benthic organisms.

Overall, the sub-cm modifications caused by *Chondrites* have wide-ranging implications beyond mineral redistribution and trace metals dilution within organic-rich sediments. *Chondrites*-producers exert significant influences on biogeochemical processes, carbon and trace metals cycling, and the fate of organic carbon in deep-marine environments, highlighting the intricate and complex interplay between biological activity (i.e. bioturbation), sedimentary processes, and carbon and trace metal dynamics. Therefore, understanding the impacts of *Chondrites* bioturbation on sedimentary biogeochemistry by assessing its effect on trace metals distribution and OM preservation within the sediments is crucial for (i) accurately interpreting past oceanographic events (in particular deoxygenation events) from deep-sea records, and (ii) evaluating its potential impacts on carbon and trace metals cycling, as well as carbon sequestration in marine sediments.

CRediT authorship contribution statement

Ricardo D. Monedero-Contreras: Conceptualization, Data curation, Formal analysis, Investigation, Methodology, Visualization, Writing – original draft, Writing – review & editing. **Francisco J. Rodríguez-Tovar:** Funding acquisition, Supervision, Validation, Writing – review & editing. **Francisca Martínez-Ruiz:** Funding acquisition, Resources, Supervision, Validation, Writing – original draft.

Declaration of competing interest

The authors declare that they have no known competing financial interests or personal relationships that could have appeared to influence the work reported in this paper.

Data availability

Data will be made available on request.

Acknowledgments

This study has been funded by Grants PID2019-104625RB-100, PID2019-104624RB-I00 and TED2021-131697B-C22 through MCIN/AEI/ 10.13039/501100011033, Grants FEDER/Junta de Andalucía P18-RT-3804 and P18-RT-4074, and Research Groups RNM-179 and RNM-178 by Junta de Andalucía. We thank Prof. Adatte from Lausanne University (Switzerland) for Rock-eval analyses and TOC measurements. We thank the Center for Scientific Instrumentation (CIC, University of Granada) for the ICP analyses, especially to Dr. Olga Cazalla for her contribution to the numerous LA-ICP-MS analyses. We are also grateful to the Ocean Drilling Program for providing the analyzed samples and to

the ODP Core Repository (Bremen, Germany) for assistance with sampling. We extend our gratitude to Jean Sanders for finally proofreading the text. Lastly, thanks to Dr. Jean-Carlos Montero-Serrano and Dr. Laurent Riquier for improving this article through their careful review, and to Dr. Fabienne Marret-Davies for his editorial work. This study is part of R. Monedero's PhD project.

Appendix A. Supplementary data

Supplementary data to this article can be found online at https://doi.org/10.1016/j.gloplacha.2024.104387.

References

Algeo, T.J., Li, C., 2020. Redox classification and calibration of redox thresholds in sedimentary systems. Geochim. Cosmochim. Acta 287, 8–26. https://doi.org/10.1016/j.gca.2020.01.055.

Algeo, T.J., Liu, J., 2020. A re-assessment of elemental proxies for paleoredox analysis. Chem. Geol. 540, 119549 https://doi.org/10.1016/j.chemgeo.2020.119549.

Algeo, T.J., Tribovillard, N., 2009. Environmental analysis of paleoceanographic systems based on molybdenum-uranium covariation. Chem. Geol. 268, 211–225. https://doi.org/10.1016/j.chemgeo.2009.09.001.

Aller, R.C., 1994. Bioturbation and remineralization of sedimentary organic matter: effects of redox oscillation. Chem. Geol. 114, 331–345. https://doi.org/10.1016/0009-2541(94)90062-0.

Amitai, Y., Ashkenazy, Y., Gildor, H., 2018. The effect of wind-stress over the Eastern Mediterranean on deep-water formation in the Adriatic Sea. Deep Sea Res. Part II Top. Stud. Oceanogr. 164, 5–13. https://doi.org/10.1016/j.dsr2.2018.11.015.

Andersen, M.B., Matthews, A., Bar-Matthews, M., Vance, D., 2020. Rapid onset of ocean anoxia shown by high U and low Mo isotope compositions of sapropel S1. Geochem. Perspect. Lett. 15, 10–14. https://doi.org/10.3929/ethz-b-000445569.

Arndt, S., Jørgensen, B., LaRowe, D.E., Middelburg, J., Pancost, R.D., Regnier, P., 2013. Quantifying the degradation of organic matter in marine sediments: a review and synthesis. Earth Sci. Rev. 123, 53–86. https://doi.org/10.1016/j.earscirev.2013.02.008.

Baucon, A., Bednarz, M., Dufour, S., Felletti, F., Malgesini, G., Neto de Carvalho, C., Niklas, K.J., Wehrmann, A., Batstone, R., Bernardini, F., Briguglio, A., Cabella, R., Cavalazzi, B., Ferretti, A., Zanzerl, H., McIlroy, D., 2020. Ethology of the trace fossil Chondrites: form, function and environment. Earth Sci. Rev. 202, 192989 https://doi.org/10.1016/j.earscirev.2019.102989.

Bea, F., 1996. Residence of REE, Y, Th and U in granites and crustal protoliths: implications for the chemistry of crustal melts. J. Petrol. 37, 521–532. https://doi.org/10.1093/petrology/37.3.521.

Bea, F., Fershtater, G.B., Montero, P., Smirnov, V.N., Molina, J.F., 2005. Deformation-driven differentiation of granitic magma: the Stepninsk pluton of the Uralides, Russia. Lithos 81, 209–233. https://doi.org/10.1016/j.lithos.2004.10.004.

Behar, F., Beaumont, V., Penteado, H.L.B., 2001. Rock-Eval 6 technology: performances and developments. Oil Gas Sci. Technol. 56, 111–134. https://doi.org/10.2516/ogst:2001013.

Benkovitz, A., Matthews, A., Teutsch, N., Poulton, S.W., Bar-Matthews, M., Almogi-Labin, A., 2020. Tracing water-column euxinia in Eastern Mediterranean Sapropels S5 and S7. Chem. Geol. 545, 119627 https://doi.org/10.1016/j.chemgeo.2020.119627.

Berner, R.A., 1981. A new geochemical classification of sedimentary environments. J. Sediment. Res. 51, 359–365. https://doi.org/10.1306/212F7C7F-2B24-11D7-8648000102C1865D.

Bishop, J., 1988. The barite-opal-organic carbon association in oceanic particulate matter. Nature 332, 341–343. https://doi.org/10.1038/332341a0.

Bromley, R.G., 1996. Trace fossils: biology, taphonomy and applications, 2nd ed. Chapman & Hall, London. Geol. Mag. 134, 409–421. https://doi.org/10.1017/S0016756897316987.

Bromley, R.G., Ekdale, A.A., 1984. Chondrites: a trace fossil indicator of anoxia in sediments. Science 224, 872–874. https://www.jstor.org/stable/1692291.

Buatois, L.A., Mángano, M.G., 2016. Ichnology: Organism-Substrate Interactions in Space and Time. Cambridge University Press, Cambridge/New York. https://doi.org/10.1017/CBO9780511975622.

Calvert, S.E., Pedersen, T.F., 1993. Geochemistry of recent oxic and anoxic sediments: implications for the geological record. Mar. Geol. 113, 67–88. https://doi.org/10.1016/0025-3227(93)90150-T.

Calvert, S.E., Pedersen, T.F., 2007. Chapter fourteen elemental proxies for palaeoclimatic and palaeoceanographic variability in marine sediments: interpretation and application. Dev. Mar. Geo. 1, 567–644. https://doi.org/10.1016/S1572-5480(07)01019-6.

Chang, J., Li, Y., Lu, H., 2022. The morphological characteristics of authigenic pyrite formed in marine sediments. J. Mar. Sci. Eng. 10, 1533. https://doi.org/10.3390/jmse10101533.

Crusius, J., Calvert, S., Pedersen, T., Sage, D., 1996. Rhenium and molybdenum enrichments in sediments as indicators of oxic, suboxic, and sulfidic conditions of deposition. Earth Planet. Sci. Lett. 145, 65–78. https://doi.org/10.1016/S0012-821X(96)00204-X.

Dando, P.R., Southward, A.J., Southward, E.C., 2004. Rates of sediment sulphide oxidation by the bivalve mollusc Thyasira sarsi. Mar. Ecol. Prog. Ser. 280, 181–187.

Dorador, J., Rodríguez-Tovar, F.J., 2015. Ichnofabric characterization in cores: a method of digital image treatment. Ann. Soc. Geol. Pol. 85, 465–471. https://doi.org/10.14241/asgp.2015.010.

Dorador, J., Rodríguez-Tovar, F.J., 2017. High-resolution image treatment in ichnological core analysis: initial steps, advances and prospects. Earth Sci. Rev. 177, 226–237. https://doi.org/10.1016/j.earscirev.2017.11.020.

Dorador, J., Rodríguez-Tovar, F.J., 2018. High-resolution image treatment in ichnological core analysis: initial steps, advances and prospects. Earth Sci. Rev. 177, 226–237. https://doi.org/10.1016/j.earscirev.2017.11.020.

Dorador, J., Rodríguez-Tovar, F.J., Hernández-Molina, F., Stow, D., Zarikian, C., Acton, G., Bahr, A., Balestra, B., Ducassou, E., Flood, R., Flores, J.A., Furota, S., Grunert, P., Hodell, D., Jiménez-Espejo, F., Kim, J.K., Krissek, L., Kuroda, J., Li, B., Xuan, C., 2014a. Quantitative estimation of bioturbation based on digital image analysis. Mar. Geol. 349, 55–60. https://doi.org/10.1016/j.margeo.2014.01.003.

Dorador, J., Rodríguez-Tovar, F.J., IODP Expedition 339 Scientists, 2014b. Digital image treatment applied to ichnological analysis of marine core sediments. Facies 60, 39–44. https://doi.org/10.1007/s10347-013-0383-z.

Dufour, S.C., Felbeck, H., 2003. Sulphide mining by the superextensile foot of symbiotic thyasirid bivalves. Nature 426 (6962), 65–67. https://doi.org/10.1038/nature02095.

Emeis, K.C., Robertson, A.H.F., Richter, C., Shipboard Scientific Party, 1996. Proc. ODP, Init. Repts., 160: College Station, TX (Ocean Drilling Program). https://doi.org/10.2973/odp.proc.ir.160.1996.

Emeis, K.C., Sakamoto, T., Wehausen, R., Brumsack, H.J., 2000. The sapropel record of the eastern Mediterranean Sea - results of Ocean Drilling Program Leg 160. Palaeogeogr. Palaeoclimatol. Palaeoecol. 158, 371–395. https://doi.org/10.1016/S0031-0182(00)00059-6.

Fernández-Martínez, J., Rodríguez-Tovar, F.J., Piñuela, L., Martínez-Ruiz, F., García-Ramos, J.C., 2021. Bottom- and pore-water oxygenation during the early Toarcian Oceanic Anoxic Event (T-OAE) in the Asturian Basin (N Spain): Ichnological information to improve facies analysis. Sediment. Geol. 419, 105909 https://doi.org/10.1016/j.sedgeo.2021.105909.

Filippidi, A., de Lange, G.J., 2019. Eastern Mediterranean Deep Water Formation during Sapropel S1: a reconstruction using geochemical records along a bathymetric transect in the Adriatic Outflow Region. Paleoceanogr. Paleoclimatol. 34, 409–429. https://doi.org/10.1029/2018PA003459.

Gallego-Torres, D., Martinez-Ruiz, Lange, G., Jiménez-Espejo, F., Ortega-Huertas, M., 2007a. Trace-elemental derived paleoceanographic and paleoclimatic conditions for Pleistocene Eastern Mediterranean sapropels. Palaeogeogr. Palaeoclimatol. Palaeoecol. 293, 76–89. https://doi.org/10.1016/j.palaeo.2010.05.001.

Gallego-Torres, D., Martinez-Ruiz, F., Jiménez-Espejo, F., Ortega-Huertas, M., 2007b. Pliocene-Holocene evolution of depositional conditions in the eastern Mediterranean: Role of anoxia vs. productivity at time of sapropel deposition. Palaeogeogr. Palaeoclimatol. Palaeoecol. 246, 424–439. https://doi.org/10.1016/j.palaeo.2006.10.008.

Gallego-Torres, D., Martinez-Ruiz, F., De Lange, G.J., Jimenez-Espejo, F.J., Ortega-Huertas, M., 2010. Trace-elemental derived paleoceanographic and paleoclimatic conditions for Pleistocene Eastern Mediterranean sapropels. Palaeogeogr. Palaeoclimatol. Palaeoecol. 293, 76–89. https://doi.org/10.1016/j.palaeo.2010.05.001.

Green, A.S., Chandler, G.T., 1994. Meiofaunal bioturbation effects on the partitioning of sediment-associated cadmium. J. Exp. Mar. Biol. Ecol. 180, 59–70. https://doi.org/10.1016/0022-0981(94)90079-5.

Hammer, Ø., Harper, D.A.T., Ryan, P.D., 2001. PAST: paleontological statistics software package for education and data analysis. Palaeontol. Electron. 4, 1–9. http://palaeo-electronica.org/2001_1/past/issue1_01.htm.

Hantsoo, K., Gomes, M., Malkin, S., Brenner, D., Kenney, W.F., 2023. Sedimentary pyrite formation in a seasonally oxygen-stressed estuary: potential imprints of microbial ecology and position-specific isotope fractionation. Eur. J. Vasc. Endovasc. Surg. 128 https://doi.org/10.1029/2022JG007324 e2022JG007324.

Helz, G.R., Vorlicek, T.P., 2019. Precipitation of molybdenum from euxinic waters and the role of organic matter. Chem. Geol. 509, 178–193. https://doi.org/10.1016/j.chemgeo.2019.02.001.

Helz, G.R., Miller, C.V., Charnock, J.M., Mosselmans, J.F.W., Pattrick, R.A.D., Garner, C. D., Vaughan, D.J., 1996. Mechanism of molybdenum removal from the sea and its concentration in black shales: EXAFS evidence. Geochim. Cosmochim. Acta 60, 3631–3642. https://doi.org/10.1016/0016-7037(96)00195-0.

Hennekam, R., Jilbert, T., Schnetger, B., de Lange, G.J., 2014. Solar forcing of Nile discharge and sapropel S1 formation in the early to middle Holocene eastern Mediterranean. Paleoceanography 29, 343–356. https://doi.org/10.1002/2013PA002553.

Hennekam, R., Jilbert, T., Mason, P.R.D., de Lange, G.J., Reichart, G.-J., 2015. High-resolution line-scan analysis of resin-embedded sediments using laser ablation-inductively coupled plasma-mass spectrometry (LA-ICP-MS). Chem. Geol. 403, 42–51. https://doi.org/10.1016/j.chemgeo.2015.03.004.

Hennekam, R., van der Bolt, B., van Nes, E.H., de Lange, G.J., Scheffer, M., Reichart, G.J., 2020. Early-warning signals for marine anoxic events. Geophys. Res. Lett. 47 https://doi.org/10.1029/2020GL089183.

Hilbrecht, H., Dahmer, D.D., 1994. Sediment dynamics during the Cenomanian-Turonian (cretaceous) oceanic anoxic event in Northwestern Germany. Facies 30, 63–83. https://doi.org/10.1007/BF02536890.

Hilgen, F.J., 1991. Astronomical calibration of Gauss to Matuyama sapropels in the Mediterranean and implication for the geomagnetic polarity time scale. Earth Planet. Sci. Lett. 104, 226–244. https://doi.org/10.1016/0012-821X(91)90206-W.

Jilbert, T., de Lange, G., Reichart, G.J., 2008. Fluid displacive resin embedding of laminated sediments: preserving trace metals for high-resolution paleoclimate

investigations. Limnol. Oceanogr. Methods 6, 16–22. https://doi.org/10.4319/lom.2008.6.16.
Jilbert, T., Reichart, G.J., Mason, P., de Lange, G.J., 2010. Short-time-scale variability in ventilation and export productivity during the formation of Mediterranean sapropel S1. Paleoceanography 25, PA4232. https://doi.org/10.1029/2010PA001955.
Jørgensen, B.B., Nelson, D., 2004. Sulfide oxidation in marine sediments: geochemistry meets microbiology. Spec. Pap. Geol. Soc. Am. 379, 63–81. https://doi.org/10.1130/0-8137-2379-5.63.
Jørgensen, B.B., Glud, R.N., Holby, O., 2005. Oxygen distribution and bioirrigation in Artic fjord sediments (Svalbard, Barents Sea). Mar. Ecol. Prog. Ser. 292, 85–95. https://doi.org/10.3354/meps292085.
Jørgensen, B.B., Wenzhöfer, F., Egger, M., Glud, R.N., 2022. Sediment oxygen consumption: Role in the global marine carbon cycle. Earth Sci. Rev. 228, 103987 https://doi.org/10.1016/j.earscirev.2022.103987.
Jovanovic, Z., Larsen, M., Quintana, C.O., Kristensen, E., Glud, R.N., 2014. Oxygen dynamics and porewater transport in sediments inhabited by the invasive polychaete Marenzelleria viridis. Mar. Ecol. Prog. Ser. 504, 181–192. https://doi.org/10.3354/meps10737.
Kamp-Nielsen, L., Mejer, H., Jørgensen, S.E., 1982. Modelling the influence of bioturbation on the vertical distribution of sedimentary phosphorus in L. Esrom. Hydrobiologia 91, 197–206. https://doi.org/10.1007/BF00940110.
Knaust, D., 2017. Atlas of Trace Fossils in Well Core: Appearance, Taxonomy and Interpretation. Springer, Alphen aan den Rijn. https://doi.org/10.1007/978-3-319-49837-9.
Lafargue, E., Marquis, F., Pillot, D., 1998. Rock-Eval 6 applications in hydrocarbon exploration, production, and soil contamination studies. Oil Gas Sci. Technol. 53, 421–437. https://doi.org/10.2516/ogst:1998036.
de Lange, G.J., Thomson, J., Reitz, A., Slomp, C.P., Speranza Principato, M., Erba, E., Corselli, C., 2008. Synchronous basin-wide formation and redox-controlled preservation of a Mediterranean sapropel. Nat. Geosci. 1, 606–610. https://doi.org/10.1038/ngeo283.
Laskar, J. Joutel, F., Boudin, F., 1993. Orbital, precessional and insolation quantities for the Earth from -20 Myr to +10 Myr. Astronphys. 270, 522-533.
Lefèvre, C.T., Bazylinski, D.A., 2013. Ecology, diversity, and evolution of magnetotactic bacteria. Microbiol. Mol. Biol. Rev. 77 (3), 497–526. https://doi.org/10.1128/MMBR.00021-13.
Lin, Q., Wang, J., Algeo, T.J., Sun, F., Lin, R., 2016. Enhanced framboidal pyrite formation related to anaerobic oxidation of methane in the sulfate-methane transition zone of the northern South China Sea. Mar. Geol. 379, 100–108. https://doi.org/10.1016/j.margeo.2016.05.016.
Little, S.H., Vance, D., Lyons, T.W., McManus, J., 2015. Controls on trace metal authigenic enrichment in reducing sediments: insights from modern oxygen-deficient settings. Am. J. Sci. 315, 77–119. https://doi.org/10.2475/02.2015.01.
Liu, Z., Chen, D., Zhang, J., Lü, X., Wang, Z., Liao, W., Shi, X., Tang, J., Xie, G., 2019. Pyrite morphology as an indicator of paleoredox conditions and shale gas content of the Longmaxi and Wufeng Shales in the middle Yangtze Area, South China. Minerals 9, 428. https://doi.org/10.3390/min9070428.
Löhr, S.C., Kennedy, M.J., 2015. Micro-trace fossils reveal pervasive reworking of Pliocene sapropels by low-oxygen-adapted benthic meiofauna. Nat. Commun. 6, 1–8. https://doi.org/10.1038/ncomms7589.
Lourens, L.J., Antonarakou, A., Hilgen, F.J., van Hoof, A.A.M., Vergnaud-Grazzini, C., Zachariasse, W.J., 1996. Evaluation of the Plio-Pleistocene astronomical time-scale. Paleoceanography 11, 391–413. https://doi.org/10.1029/96PA01125.
Löwemark, L., Lin, Y., Chin, H.F., Yang, T.N., Beier, C., Werner, F., Lee, C.Y., Song, S.R., Kao, S.J., 2006. Sapropel burn-down and ichnological response to late Quaternary sapropel formation in two ~ 400 ky records from the eastern Mediterranean Sea. Palaeogeogr. Palaeoclimatol. Palaeoecol. 239, 406–425. https://doi.org/10.1016/j.palaeo.2006.02.013.
Martínez-Ruiz, F., Kastner, M., Paytan, A., Ortega-Huertas, M., Bernasconi, S.M., 2000. Geochemical evidence for enhanced productivity during S1 sapropel deposition in the eastern Mediterranean. Paleoceanography 15, 200–209. https://doi.org/10.1029/1999PA000419.
Martínez-Ruiz, F., Jroundi, F., Paytan, A., Guerra-Tschuschke, I., Abad, M.M., González-Muñoz, M.T., 2018. Barium bioaccumulation by bacterial biofilms and implications for Ba cycling and use of Ba proxies. Nat. Commun. 9, 1619. https://doi.org/10.1038/s41467-018-04069-z.
Martínez-Ruiz, F., Paytan, A., Gonzalez-Muñoz, M.T., Jroundi, F., Abad, M.M., Lam, P., Bishop, J.K.B., Horner, T.J., Morton, P., Kastner, M., 2019. Barite formation in the ocean: Origin of amorphous and crystalline precipitates. Chem. Geol. 511, 441–451. https://doi.org/10.1016/j.chemgeo.2018.09.011.
Martínez-Ruiz, F., Paytan, A., Gonzalez-Muñoz, M.T., Jroundi, F., Abad, M.M., Lam, P.J., Horner, T.J., Kastner, M., 2020. Barite precipitation on suspended organic matter in the mesopelagic zone. Front. Earth-Sci. 8, 567714 https://doi.org/10.3389/feart.2020.567714.
Matthews, A., Azrieli-Tal, I., Benkovitz, A., Bar-Matthews, M., Vance, D., Poulton, S.W., Teutsch, N., Almogi-Labin, A., Archer, C., 2017. Anoxic development of sapropel S1 in the Nile Fan inferred from redox sensitive proxies, Fe speciation, Fe and Mo isotopes. Chem. Geol. 475, 24–39. https://doi.org/10.1016/j.chemgeo.2017.10.028.
McManus, J., Berelson, W.M., Klinkhammer, G.P., Hammond, D.E., Holm, C., 2005. Authigenic uranium: relationship to oxygen penetration depth and organic carbon rain. Geochim. Cosmochim. Acta 69, 95–108. https://doi.org/10.1016/j.gca.2004.06.023.
Meadows, P.S., Meadows, A., Zoological Society of London, 1991. The Environmental Impact of Burrowing Animals and Animal Burrows: The Proceedings of a Symposium Held at the Zoological Society of London on 3rd and 4th May 1990. Published for the Zoological Society of London by Clarendon Press, Oxford. http://www.loc.gov/catdir/enhancements/fy0635/91024767-t.html.
Meysman, F.J.R., Galaktionov, O.S., Gribsholt, B., Middelburg, J.J., 2006. Bioirrigation in permeable sediments: Advective pore-water transport induced by burrow ventilation. Limnol. Oceanogr. 51, 142–156. https://doi.org/10.4319/lo.2006.51.1.0142.
Millot, C., Taupier-Letage, I., 2005. Circulation in the Mediterranean Sea. In: Saliot, A. (Ed.), The Mediterranean Sea, Handb. Environ. Chem, 5. Springer, Berlin, Heidelberg, pp. 26–66. https://doi.org/10.1007/b107143.
Moens, T., Santos, G.A.P., Thompson, F., Swings, J., Fonsêca-Genevois, V., Vincx, M., De Mesel, I., 2005. Do nematode mucus secretions affect bacterial growth? Aquat. Microb. Ecol. 40, 77–83. https://doi.org/10.3354/ame040077.
Monaco, P., Rodríguez-Tovar, F.J., Uchman, A., 2012. Ichnological analysis of lateral environmental heterogeneity within the Bonarelli Level (uppermost Cenomanian) in the classical localities near Gubbio, Central Apennines, Italy. PALAIOS 27, 48–54. https://doi.org/10.2110/palo.2011.p11-018r.
Monaco, P., Rodríguez-Tovar, F.J., Uchman, A., 2016. The stratigraphic record of gubbio: integrated stratigraphy of the late Cretaceous-Paleogene Umbria-Marche Pelagic Basin. GSA Spec. Pap. 524, 97–103. https://doi.org/10.1130/SPE524.
Monedero-Contreras, R.D., Martínez-Ruiz, F., Rodríguez-Tovar, F.J., 2023a. Role of climate variability on deep-water dynamics and deoxygenation during sapropel deposition: New insights from a palaeoceanographic empirical approach. Palaeogeogr. Palaeoclimatol. Palaeoecol. 622, 111601 https://doi.org/10.1016/j.palaeo.2023.111601.
Monedero-Contreras, R.D., Martínez-Ruiz, F., Rodríguez-Tovar, F.J., 2023b. Evidence of postdepositional remobilization of redox-sensitive metals across sapropel boundaries: new insights from LA-ICP-MS and EDX mapping analyses. Chem. Geol. 121643 https://doi.org/10.1016/j.chemgeo.2023.121643.
Monedero-Contreras, R.D., Martínez-Ruiz, F., Rodríguez-Tovar, F.J., de Lange, G., 2024. Redox geochemical signatures in Mediterranean sapropels: Implications to constrain deoxygenation dynamics in deep-marine settings. Palaeogeogr. Palaeoclimatol. Palaeoecol. 634, 111953 https://doi.org/10.1016/j.palaeo.2023.111953.
Montero-Serrano, J.C., Föllmi, K.B., Adatte, T., Spangenberg, J.E., Tribovillard, N., Fantasia, A., Suan, G., 2015. Continental weathering and redox conditions during the early Toarcian Oceanic Anoxic Event in the northwestern Tethys: Insight from the Posidonia Shale section in the Swiss Jura Mountains. Palaeogeogr. Palaeoclimatol. Palaeoecol. 429, 83–99. https://doi.org/10.1016/j.palaeo.2015.03.043.
Morford, J.L., Emerson, S.R., Breckel, E.J., Kim, S.H., 2005. Diagenesis of oxyanions (V, U, Re, and Mo) in pore waters and sediments from a continental margin. Geochim. Cosmochim. Acta 69, 5021–5032. https://doi.org/10.1016/j.gca.2005.05.015.
Neira, C., Sellanes, J., Levin, L.A., Arntz, W.E., 2001. Meiofaunal distributions on the Peru margin: relationship to oxygen and organic matter availability. Deep Sea Res. Part I Oceanogr. Res. Pap. 48, 2453–2472. https://doi.org/10.1016/S0967-0637(01)00018-8.
Nijenhuis, I.A., Bosch, H.J., Damsté, J.S., Brumsack, H.J., de Lange, G.J., 1999. Organic matter and trace element rich sapropels and black shales: a geochemical comparison. Earth Planet. Sci. Lett. 169, 277–290. https://doi.org/10.1016/S0012-821X(99)00083-7.
Ordoñez, L., Vogel, H., Sebag, D., Ariztegui, D., Adatte, T., Russell, J.M., Kallmeyer, J., Vuillemin, A., Friese, A., Crowe, S.A., Bauer, K.W., Simister, R., Henny, C., Nomosatryo, S., Bijaksana, S., 2019. Empowering conventional Rock-Eval pyrolysis for organic matter characterization of the siderite-rich sediments of Lake Towuti (Indonesia) using End-Member Analysis. Org. Geochem. 134, 32–44. https://doi.org/10.1016/j.orggeochem.2019.05.002.
van Os, B.J.H., Middelburg, J.J., de Lange, G.J., 1991. Possible diagenetic mobilization of barium in sapropelic sediment from the eastern Mediterranean. Mar. Geol. 100, 125–136. https://doi.org/10.1016/0025-3227(91)90229-W.
Passier, H.F., Middelburg, J.J., van Os, B.J.H., de Lange, G.J., 1996. Diagenetic pyritisation under eastern Mediterranean sapropels caused by downward sulphide diffusion. Geochim. Cosmochim. Acta 60, 751–776. https://doi.org/10.1016/0016-7037(95)00419-X.
Passier, H.F., Middelburg, J., de Lange, G., Böttcher, M., 1997. Pyrite contents, microtextures, and sulfur isotopes in relation to formation of the youngest eastern Mediterranean sapropel. Geology 25, 519–522. https://doi.org/10.1130/0091-7613(1997)025<0519:PCMASI>2.3.CO;2.
Passier, H.F., Bosch, H.J., Nijenhuis, I., Lourens, L., Böttcher, M., Leenders, A., Sinninghe-Damste, J., de Lange, G., de Leeuw, J., 1999. Sulphic Mediterranean surface waters during Pliocene sapropel formation. Nature 397, 146–149. https://doi.org/10.1038/16441.
Paul, K.M., van Heldmond, N.A.G.M., Slomp, C.P., Jokinen, S.A., Virtasalo, J.J., Filipsson, H.L., Jilbert, T., 2023. Sedimentary molybdenum and uranium: improving proxies for deoxygenation in coastal depositional environments. Chem. Geol. 615, 121203 https://doi.org/10.1016/j.chemgeo.2022.121203.
Paytan, A., Griffith, E.M., 2007. Marine barite: recorder of variations in ocean export productivity. Deep Sea Res. Part Top. Stud. Oceanogr. 54, 687–705. https://doi.org/10.1016/j.dsr2.2007.01.007.
Paytan, A., Mearon, S., Cobb, K., Kastner, M., 2002. Origin of marine Barite deposits: Sr and S isotope characterization. Geology 30, 747–750. https://doi.org/10.1130/0091-7613(2002)030<0747:oombds>2.0.co;2.
Paytan, A., Martinez-Ruiz, F., Eagle, M., Ivy, A., Wankel, S., 2004. Using sulfur isotopes to elucidate the origin of barite associated with high organic matter accumulation events in marine sediments. Geol. Soc. Am. Spec. Pap. 379, 151–160. https://doi.org/10.1130/0-8137-2379-5.151.
Pearce, N.J.G., Perkins, W.T., Westgate, J.A., Gorton, M.P., Jackson, S.E., Neal, C.R., Chenery, S.P., 2007. A compilation of new and published major and trace element data for NIST SRM 610 and NIST SRM 612 Glass Reference Materials. Geostandards

Newslett. J. Geostand. Geoanal. 21, 115–144. https://doi.org/10.1111/j.1751-908X.1997.tb00538.x.
Phillips, C., McIlroy, D., 2010. Ichnofabrics and Biologically Mediated changes in Clay Mineral Assemblages from a Deep-water, Fine-grained, Calcareous Sedimentary Succession: an example from the Upper cretaceous Wyandot Formation, Offshore Nova Scotia. Bull. Can. Petrol. Geol. 58, 203–218. https://doi.org/10.2113/gscpgbull.58.3.203.
POEM Group, 1992. General circulation of the eastern Mediterranean Sea. Earth Sci. Rev. 32, 285–308. https://doi.org/10.1016/0012-8252(92)90002-B.
Pruysers, P.A., de Lange, G.J., Middelburg, J.J., 1991. Geochemistry of eastern Mediterranean sediments: primary sediment composition and diagenetic alterations. Mar. Geol. 100, 137–154. https://doi.org/10.1016/0025-3227(91)90230-2.
Pruysers, P.A., de Lange, G.J., Middelburg, J.J., Hydes, D.J., 1993. The diagenetic formation of metal-rich layers in sapropel-conatining sediments in the eastern Mediterranean. Geochim. Cosmochim. Acta 57, 527–536. https://doi.org/10.1016/0016-7037(93)90365-4.
Reitz, A., Thomson, J., de Lange, G.J., Hensen, C., 2006. Source and development of large manganese enrichments above eastern Mediterranean sapropel S1. Paleoceanography 21. https://doi.org/10.1029/2005PA001169. PA3007.
Rodríguez-Tovar, F.J., 2021a. Ichnology of the Toarcian Oceanic Anoxic Event: an underestimated tool to assess palaeoenvironmental interpretations. Earth Sci. Rev. 216, 103579 https://doi.org/10.1016/j.earscirev.2021.103579.
Rodríguez-Tovar, F.J., 2021b. Toarcian Oceanic Anoxic Event in the Iberian Massif: the ichnological record. Geol. Today 37, 134–140. https://doi.org/10.1111/gto.12361.
Rodríguez-Tovar, F.J., 2022. Ichnological analysis: a tool to characterize deep-marine processes and sediments. Earth Sci. Rev. 228, 104014 https://doi.org/10.1016/j.earscirev.2022.104014.
Rodríguez-Tovar, F.J., Uchman, A., 2010. Ichnofabric evidence for the lack of bottom anoxia during the lower Toarcian Oceanic Anoxic Event in the Fuente de la Vidriera section, Betic Cordillera, Spain. PALAIOS 25, 576–587. https://doi.org/10.2110/palo.2009.p09-153r.
Rodríguez-Tovar, F.J., Uchman, A., 2011. Ichnological data as a useful tool for deep-sea environmental characterization: a brief overview and an application to recognition of small-scale oxygenation changes during the Cenomanian-Turonian anoxic event. Geo-Mar. Lett. 31, 525–536. https://doi.org/10.1007/s00367-011-0237-z.
Rodríguez-Tovar, F.J., Uchman, A., 2017. The Faraoni event (latest Hauterivian) in ichnological record: the Rio Argos section of southern Spain. Cretac. Res. 79, 109–121. https://doi.org/10.1016/j.cretres.2017.07.018.
Rodríguez-Tovar, F.J., Martínez-Ruiz, F., Bernasconi, S.M., 2004. Carbon isotope evidence for the timing of the Cretaceous-Palaeogene macrobenthic colonization at the Agost section (Southeast Spain). Palaeogeogr. Palaeoclimatol. Palaeoecol. 203, 65–72. https://doi.org/10.1016/S0031-0182(03)00660-6.
Rodríguez-Tovar, F.J., Martínez-Ruiz, F., Bernasconi, S.M., 2006. Use of high resolution ichnological and stable isotope data for assessing completeness of a K-P boundary section, Agost, Spain. Palaeogeogr. Palaeoclimatol. Palaeoecol. 237, 137–146. https://doi.org/10.1016/j.palaeo.2005.11.019.
Rodríguez-Tovar, F.J., Uchman, A., Martín-Algarra, A., 2009a. Oceanic anoxic event at the Cenomanian-Turonian boundary interval (OAE-2): ichnological approach from the Betic Cordillera, southern Spain. Lethaia 42, 407–417. https://doi.org/10.1111/j.1502-3931.2009.00159.x.
Rodríguez-Tovar, F.J., Uchman, A., Martín-Algarra, A., O'Dogherty, L., 2009b. Nutrient spatial variation during intrabasinal upwelling at the Cenomanian-Turonian oceanic anoxic event in the westernmost Tethys: an ichnological and facies approach. Sediment. Geol. 215, 83–93. https://doi.org/10.1016/j.sedgeo.2009.01.006.
Rodríguez-Tovar, F.J., Uchman, A., Reolid, M., Sánchez-Quiñónez, C.A., 2020. Ichnological analysis of the Cenomanian-Turonian boundary interval in a collapsing slope setting: a case from the Rio Fardes section, southern Spain. Cretac. Res. https://doi.org/10.1016/j.cretres.2019.104262.
Rodríguez-Tovar, F.J., Dorador, J., Zuchuat, V., Planke, S., Hammer, Ø., 2021. Response of macrobenthic trace maker community to the end-Permian mass extinction in Central Spitsbergen, Svalbard. Palaeogeogr. Palaeoclimatol. Palaeoecol. 581, 110637 https://doi.org/10.1016/j.palaeo.2021.110637.
Rohling, E.J., Marino, G., Grant, K.M., 2015. Mediterranean climate and oceanography, and the periodic development of anoxic events (sapropels). Earth Sci. Rev. 143, 62–97. https://doi.org/10.1016/j.earscirev.2015.01.008.
Rysgaard, S., Christensen, P.B., Sørensen, M.V., Funch, P., Berg, P., 2000. Marine meiofauna, carbon and nitrogen mineralization in sandy and soft sediments of Disko Bay, West Greenland. Aquat. Microb. Ecol. 21, 59–71. https://doi.org/10.3354/ame021059.
van Santvoort, P.J.M., de Lange, G.J., Langereis, C.G., Dekkers, M.J., Paterne, M., 1997. Geochemical and Paleomagnetic evidence for the occurrence of "missing" sapropels in eastern Mediterranean sediments. Paleoceanography 12, 773–786. https://doi.org/10.1029/97PA01351.
Savrda, C.E., Bottjer, D.J., 1984. Trace-fossil model for reconstruction of paleo-oxygenation in bottom waters. Geology 14, 3–6. https://doi.org/10.1130/0091-7613(1986)14<3:TMFROP>2.0.CO;2.
Scheiderich, K., Zerkl, A.L., Helz, G.R., Farquhar, J., Walker, R.J., 2010. Molybdenum isotope, multiple sulfur isotope, and redox-sensitive element behavior in early. Pleistocene Mediterranean sapropels. Chem. Geol. 279, 134–144. https://doi.org/10.1016/j.chemgeo.2010.10.015.
Scholz, F., Siebert, C., Dale, A.W., Frank, M., 2017. Intense molybdenum accumulation in sediments underneath a nitrogenous water-column and implications for the reconstruction of paleo-redox conditions based on molybdenum isotopes. Geochim. Cosmochim. Acta 213, 400–417. https://doi.org/10.1016/j.gca.2017.06.048.
Schönfeld, J., Schiebel, R., Timm, S., 1991. The Rotpläner (Upper Cenomanian to lower Turonian) of Baddecken-stedt (North-Western Germany): lithology, geochemistry, foraminifers, and stratigraphic correlations. Meyniana 43, 73–95. https://doi.org/10.2312/meyniana.1991.43.73.
Scott, C., Lyons, T.W., 2012. Contrasting molybdenum cycling and isotopic properties in euxinic versus non-euxinic sediments and sedimentary rocks: refining the paleoproxies. Chem. Geol. 324-325, 19–27. https://doi.org/10.1016/j.chemgeo.2012.05.012.
Sosa-Montes de Oca, C., de Lange, G.J., Martínez-Ruiz, F., Rodríguez-Tovar, F.J., 2018. Application of laser ablation-ICP-MS to determine high-resolution elemental profiles across the cretaceous/Paleogene boundary at Agost (Spain). Palaeogeogr. Palaeoclimatol. Palaeoecol. 497, 128–138. https://doi.org/10.1016/j.palaeo.2018.02.012.
StataCorp, L.P., 2007. Tata Multivariate Statistics: Reference Manual. Stata Press Publication. https://www.stata.com/manuals/mv.pdf.
Sweere, T., Hennekam, R., Vance, D., Reichart, G.J., 2021. Molybdenum isotope constraints on the temporal development of sulfidic conditions during Mediterranean sapropel intervals. Geochem. Perspect. Lett. 17, 16–20. https://doi.org/10.7185/geochemlet.2108.
Tachikawa, K., Vidal, L., Cornuault, M., Garcia, M., Pothin, A., Sonzogni, C., Bard, E., Menot, G., Revel, M., 2015. Eastern Mediterranean Sea circulation inferred from the conditions of S1 sapropel deposition. Clim. Past 11 (855–867), 2015. https://doi.org/10.5194/cp-11-855-2015.
Taylor, A.M., Gawthorpe, R.L., Goldring, R., 1993. Description and analysis of bioturbation and ichnofabric. J. Geol. Soc. Lond. 150, 141–148. https://doi.org/10.1144/gsjgs.150.1.0141.
Tribovillard, N., Algeo, T.J., Lyons, T., Riboulleau, A., 2006. Trace metals as paleoredox and paleoproductivity proxies: an update. Chem. Geol. 232, 12–32. https://doi.org/10.1016/j.chemgeo.2006.02.012.
Tribovillard, N., Lyons, T.W., Riboulleau, A., Bout-Roumazeilles, V., 2008. A possible capture of molybdenum during early diagenesis of dysoxic sediments. Bull. Soc. Geol. Fr. 179, 3–12. https://doi.org/10.2113/gssgfbull.179.1.3.
Uchman, A., Bąk, K., Rodríguez-Tovar, F.J., 2008. Ichnological record of deep-sea palaeoenvironmental changes around the Oceanic Anoxic Event 2 (Cenomanian-Turonian boundary): an example from the Barnasiówka section, Polish Outer Carpathians. Palaeogeogr. Palaeoclimatol. Palaeoecol. 262, 61–71. https://doi.org/10.1016/j.palaeo.2008.02.002.
Uchman, A., Rodríguez-Tovar, F.J., Machaniec, E., Kędzierski, M., 2013a. Ichnological characteristics of late cretaceous hemipelagic and pelagic sediments in a submarine high around the OAE-2 event: a case from the Rybie section, Polish Carpathians. Palaeogeogr. Palaeoclimatol. Palaeoecol. 370, 222–231. https://doi.org/10.1016/j.palaeo.2012.12.013.
Uchman, A., Rodríguez-Tovar, F.J., Oszczypko, N., 2013b. Exceptionally favourable life conditions for macrobenthos during the late Cenomanian OAE-2 event: ichnological record from the Bonarelli Level in the Grajcarek Unit. Polish Carpathians Cretac. Res. 46, 1–10. https://doi.org/10.1016/j.cretres.2013.08.007.
Warning, B., Brumsack, H.J., 2000. Trace metal signatures of eastern Mediterranean sapropels. Paleogeogr. Paleoclimatol. Paleoecol. 158, 293–309. https://doi.org/10.1016/S0031-0182(00)00055-9.
Weldeab, S., Menke, V., Schmiedl, G., 2014. The pace of East African monsoon evolution during the Holocene. Geophys. Res. Lett. 41, 1724–1731. https://doi.org/10.1002/2014GL059361.
Wilkin, R.T., Barnes, H.L., 1997. Formation processes of framboidal pyrite. Geochim. Cosmochim. Acta 61, 323–339. https://doi.org/10.1016/S0016-7037(96)00320-1.
Wilkin, R.T., Barnes, H.L., Brantley, S.L., 1996. The size distribution of framboidal pyrite in modern sediments: an indicator of redox conditions. Geochim. Cosmochim. Acta 60, 3897–3912. https://doi.org/10.1016/0016-7037(96)00209-8.
Wilkin, R.T., Arthur, M.A., Dean, W.E., 1997. History of water-column anoxia in the Black Sea indicated by pyrite framboid size distributions. Earth Planet. Sci. Lett. 148, 517–525. https://doi.org/10.1016/S0012-821X(97)00053-8.
Wilson, T.R.S., Thomson, J., Hydes, D.J., Colley, S., Culkin, E., Sorensen, J., 1986. Oxidation fronts in pelagic sediments: Diagenetic formation of metal-rich layers. Science 232, 972–975. https://doi.org/10.1126/science.232.4753.972.
Wu, J., Böning, P., Pahnke, K., Tachikawa, K., de Lange, G., 2016. Unraveling North-African riverine and eolian contributions to Central Mediterranean sediments during Holocene sapropel S1 formation. Quat. Sci. Rev. 152, 31–48. https://doi.org/10.1016/j.quascirev.2016.09.029.
Wu, J., Fillipidi, A., Davies, G.R., de Lange, G., 2018. Riverine supply to the eastern Mediterranean during last interglacial sapropel S5 formation: a basin-wide perspective. Chem. Geol. 485, 74–89. https://doi.org/10.1016/j.chemgeo.2018.03.037.
Wüst, G., 1961. On the vertical circulation of the Mediterranean Sea. J. Geophys. Res. 66, 3261–3271. https://doi.org/10.1029/JZ066i010p03261.
Yin, H., Zhu, Q., Aller, R.C., 2017. An irreversible planar optical sensor for multi-dimensional measurements of sedimentary H_2S. Mar. Chem. 195, 143–152. https://doi.org/10.1016/j.marchem.2017.03.005.
Zheng, Y., Anderson, R.F., van Geen, A., Fleisher, M.Q., 2002. Remobilization of authigenic uranium in marine sediments by bioturbation. Geochim. Cosmochim. Acta 66, 1759–1772. https://doi.org/10.1016/S0016-7037(01)00886-9.
Ziegler, M., Tuenter, E., Lourens, L.J., 2010. The precession phase of the boreal summer monsoon as viewed from the eastern Mediterranean (ODP Site 968). Quat. Sci. Rev. 29, 1481–1490. https://doi.org/10.1016/j.quascirev.2010.03.011.
Zirks, E., Krom, M.D., Zhu, D., Schmiedl, G., Goodman-Tchernov, B.N., 2019. ACS Earth Space Chem. 3, 2287–2297. https://doi.org/10.1021/acsearthspacechem.9b00128.